IEEE Access
Multidisciplinary | Rapid Review | Open Access Journal

Received June 2, 2022, accepted June 14, 2022, date of publication June 20, 2022, date of current version June 24, 2022.

Digital Object Identifier 10.1109/ACCESS.2022.3184421

Efficient Cable Path Optimization Based on Critical Robot Poses for Industrial Robot Arms

SHINTARO IWAMURA[1,2], YOSHIKI MIZUKAMI[2], (Member, IEEE), TAKAHIRO ENDO[3], (Member, IEEE), AND FUMITOSHI MATSUNO[3], (Senior Member, IEEE)

[1]Controller Division, Product Business Division H.Q., Software Development Department, Industrial Automation Company, Omron Corporation, Shimogyo-ku, Kyoto 600-8530, Japan
[2]Graduate School of Science and Engineering, Yamaguchi University, Ube, Yamaguchi 755-8611, Japan
[3]Department of Mechanical Engineering and Science, Kyoto University, Kyodai-katsura, Nishikyo-ku, Kyoto 615-8540, Japan

Corresponding author: Yoshiki Mizukami (mizu@yamaguchi-u.ac.jp)

ABSTRACT Although industrial robotic arms are equipped with external cables to supply electricity, gases or other materials, cable path design is a difficult and demanding task. Herein, an efficient optimization method is proposed for automating cable path design under the assumption that the robot motion path is known. The contribution of this study was to reduce the considerable computation time required for the optimization, which was a concern in our previous work. The previous method represented candidates for cable paths as a set of parameter vectors (PVs) that included cable length and guide configurations, and then selected the optimal PV that satisfies stress constraints and provided the shortest cable path. The proposed method extracted critical poses, i.e., several static robot poses that are prone to applying stress to the cable, from the joint angle time series of the motion path, and then performed attachment and motion tests. The cable geometry for the static critical poses was simulated in the attachment test, while the geometry for dynamic robot motion was simulated in the motion test in an ascending order of the cable length among the PV candidates. Experimental results showed that the computation time for cable path optimization could be significantly reduced.

INDEX TERMS Computer simulation, industrial engineering, optimal matching, path planning, robotics and automation.

I. INTRODUCTION

According to the International Federation of Robotics, the global installations of industrial robot arms were ∼380,000 units in 2020, with ∼3.0 million operational stocks of industrial robot arms [1]. With an increase in the number of robots in manufacturing scenes, new intelligent control paradigms for robot collaboration and their future applications are discussed [2], [3]. Robot arms are used in several applications including the production of electricity, electronics, food, and chemicals. End effectors and sensors are attached to the robot arm to execute numerous functions. Some examples of end effectors and sensors are motorized chucks and air chucks for realizing pick-and-place motion, adhesive spraying, and visual inspection. Electricity and gases are delivered to the end effector via external cables and tubes, respectively. Because the motion of a robot arm is complex, a cable path design, i.e., the configuration of guides for attaching cables and the cable length, is a demanding task that requires considerable effort and person-hours from engineers. Therefore, an efficient automatic optimization method is required for a cable path design.

To optimize the cable path, the geometric deformation of the cable associated with the joint angle of the robot arm must be physically simulated. The Cosserat theory [4] is a fundamental theory of micropolar elasticity that defines distinct translational and rotational degrees of freedom for each cable element. Spillmann and Teschner [5] developed a model that divides the cable into discrete one-dimensional (1D) elements along its centerline, defines the position and orientation of each cable element, and uses the finite element method to calculate the continuous deformation energy of each cable element. Grégoire and Schömer [6] separately expressed the bending and torsion energies and adopted a generalized mass–spring model. Mass–spring models to represent the deformation of objects has been used for computer

The associate editor coordinating the review of this manuscript and approving it for publication was Mohammad Alshabi.

animation since the 1980s. Baraff and Witkin [7] represented the clothes worn by animated characters as simple displacement springs. Hergenröther and Dähne [8] divided wires into rigid cylindrical segments linked with ball joints. Loock and Schömer [9] split a cable into stiff segments and used torsion springs in addition to linear and bending springs for connections between the segments. Lv *et al.* [10] applied physical models of cable harnesses with a linear spring for elongation, a bending spring for bending, and torsion springs for geometric and material torsion. A position-based dynamic framework has been proposed to increase the simulation speed and stabilize collision detection between rigid bodies [11] and implemented in physics engines such as Bullet, Havok [12], [13], and PhysX [14].

The cable-path optimization problem must be addressed based on the motion of a robot arm, i.e., the trajectory path expressed as a time series of joint angles. Generally, trajectory paths are generated by interpolating multiple waypoint poses. By operating an actual or virtual robot arm in a robot simulator, the operator creates waypoint poses. Trajectory planning is an optimization issue in which constraints are applied to reduce energy consumption, avoid collisions between the robot arm and the surrounding objects, and ensure that the robot arm is maintained within the speed and torque limits. Traditional approaches for generating trajectory paths, such as the potential method [15] and cell-division method [16], identify spatial positions that the robot can pass through while considering the locations of nearby obstacles [17]. Recently, methods based on random samplings—such as the probabilistic roadmap method [18] and rapidly exploring random tree [19]—have been widely used.

Kressin [20] and Carlson *et al.* [21] applied the simulation of cable dress-pack geometry to the trajectory path optimization problem and estimated the trajectory path which meets the stress constraints on impulse, stretch, and curvature radius, by excluding problematic alternatives for each operation executed by the robot. Hermansson *et al.* [22] proposed using an autonomous path planner to construct a collision-free path for rigid robots and then smoothed the path to account for deformations and stresses in the pack. They used a general framework for optimizing the parameters of a mechanical system subject to quasi-static motions and deformations to optimize the waypoint configuration of the trajectory path. Subsequently, they obtained the optimal robot configuration and motions using numerical solutions for a nonlinear programming problem, in which the system's static equilibrium equations hold at discrete times. Notably, the aforementioned approaches optimize the trajectory path under the condition that the configuration of the dress pack is fixed; however, the optimization of the dress-pack configuration or cable path was not discussed.

In our previous study [23], the cable path was optimized under the condition that the robot motion is known. In the study, first, the entire cable was divided into cable segments separated by guides and then, a set of parameter vectors (PVs) including the length of the cable segments and configuration of the cable guides was prepared. All PVs were analyzed on the basis of the robot motion to ensure that they meet the stress constraints proposed by Kressin [20]. The PVs that passed the motion test were grouped to construct the entire cable path. The computation time of the motion test was proportional to the product of the motion time and the number of PVs. The computation time was estimated to be >10 h based on a case study [23].

In this study, to reduce the computation time for automating the cable path design, an efficient optimization method is proposed. Here, the cable path design can be interpreted as a combinatorial optimization problem for PVs. A brute-force search is a general problem-solving method that exhaustively searches all candidate solutions to determine whether they satisfy problem requirements [24]. Although such searches can yield a global solution, the computational load becomes considerable as the number of candidate solutions increases. Consequently, general approaches for reducing the computational load have been proposed, including the branch-and-bound method [25], dynamic programming method [26], and greedy method [27]. Further, the hill-climbing approach [28] which focuses on problem-specific characteristics and best-first search [29] which maintains numerous top-level candidates in a queue have been proposed. Metaheuristic methodologies, such as evolutionary computation or closest-neighbor search methods, are also used to obtain a satisfactory solution in a short time. Evolutionary computation includes genetic algorithms [30], swarm intelligence [31], or differential evolution [32]. Furthermore, neighborhood search methods include tabu search [33] and annealing [34]. Although these approaches are effective in reducing the computational load, they do not guarantee a global solution; hence, they are considered unsuitable for the cable path design, which has a direct impact on the productivity of manufacturing facilities. Unpromising PV candidates are gradually rejected on the basis of a brute-force search by focusing on problem-specific rules of thumb.

To reduce the computation time, an efficient optimization method is proposed for automating the cable path design. Hence, a stepwise reduction of unpromising PV candidates is considered. In image processing, this stepwise reduction technique is known as a cascaded classifier. Viola *et al.* [35] proposed a fast and accurate solution that combines Haar features with a cascaded classifier for face detection. A cascade classifier comprises a concatenation of numerous strong classifiers. By distinguishing items sequentially using each strong classifier, the classifier can rapidly identify whether a target object is present at a certain position in an image. Moreover, a boosting method that parallelly combines fast weak classifiers has been proposed to construct a fast and accurate strong classifier. In particular, adaptive boosting (AdaBoost) [36] is an efficient computation method that uses adaptive weighting and parallel relearning based on the recognition rate of the classifiers in the learning process. The proposed combination of the serial cascade classifier with parallel boosting is effective and versatile and has been used in the

recognition of eyes [37], people [38], cars [39], animals [40], and other objects.

In our previous method [23], the entire cable was divided into cable segments based on a division at guide positions and multiple candidate cable paths were represented as a set of PVs that included the configuration of the guide and cable length. Then, the optimal PV providing the shortest cable path while meeting the stress constraints (impulse, stretch, and curvature radius) and robustness constraints was identified. This optimization required considerable computation time.

Therefore, in the present study, a classifier with a series–parallel structure [35], [36] is used to rapidly eliminate unpromising PV candidates and reduce the computation time required to automate the cable path design. As the main contribution of the proposed method, the following three novel concepts are introduced to reduce the computation time:

i) critical robot poses,

ii) a cascade structure in an attachment test (CSAT), and

iii) a cascade structure for cable path optimization.

Then, the entire procedure is overviewed with respect to the abovementioned concepts. The proposed method extracts several static poses of a robot that are prone to applying stress to the cable from the joint angle time series of the trajectory path as i) critical poses and then performs attachment and motion tests for determining which PVs or their combinations satisfy the stress constraints. The attachment test simulates cable geometries for static critical poses and uses ii) CSAT to save computation time, while the motion test simulates cable geometries for dynamic robot motion in an ascending order of cable path length among PV candidates. In the context of only PV candidates that pass the attachment test, being eligible for the motion test, the concatenation of the two tests is referred to as iii) a cascade structure for cable path optimization.

The remainder of this paper is organized as follows. In Section II, an efficient optimization of the cable path is conducted. In Section III, the optimal PV obtained via a simulation is validated. In Section IV, the effectiveness of the proposed method is verified by performing experiments on an actual robot arm. Finally, in Section V, this study is summarized and possible future work is discussed.

II. PROPOSED METHOD

Herein, a framework is proposed to considerably reduce the computation time required for automatically designing cable paths for a given robot motion. In our previous study [23], a set of PVs was defined, including the length of cable segments and the configuration of cable guides, and the optimal PVs from the candidate set were determined through motion tests under the condition that the robot arm motion was known. However, in the motion test, the computation time was related to the product of the motion time and the number of PVs, indicating that a considerable amount of time is required to obtain optimal PVs. As explained in the previous section, the main contribution of the proposed method includes three novel concepts that are explained in detail below.

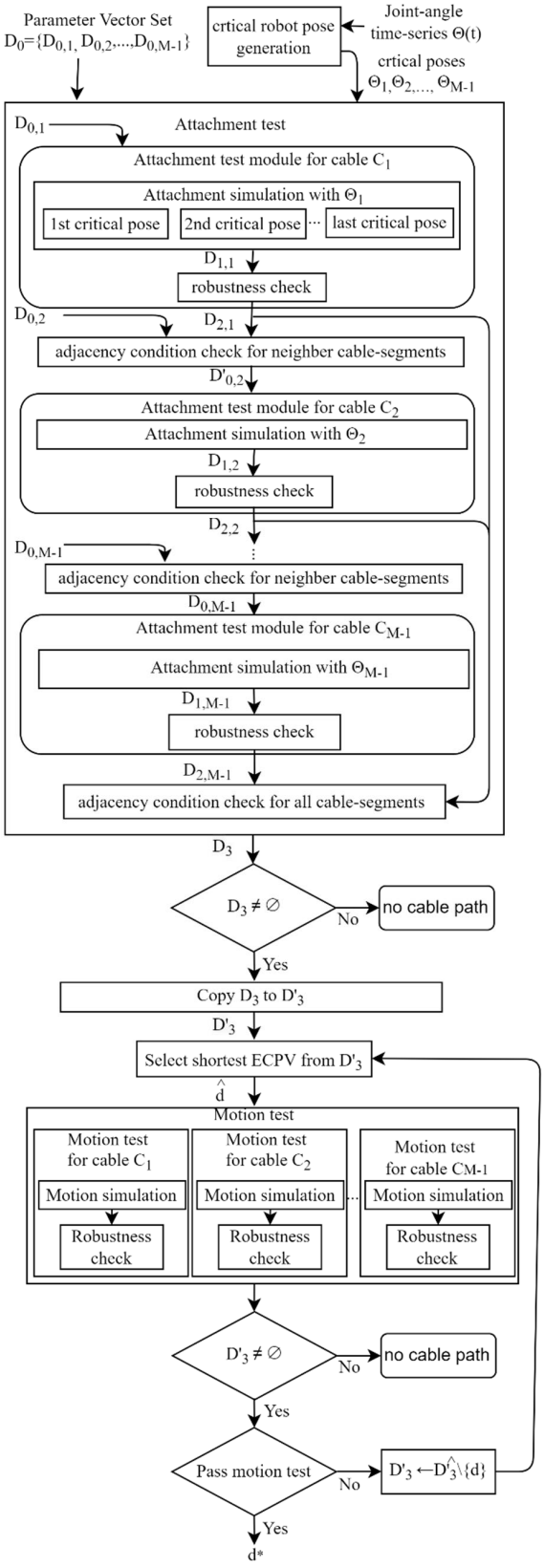

FIGURE 1. Optimization procedure in robot arm cable path planning.

In the proposed method, the computation time required for the cable path optimization is drastically reduced by

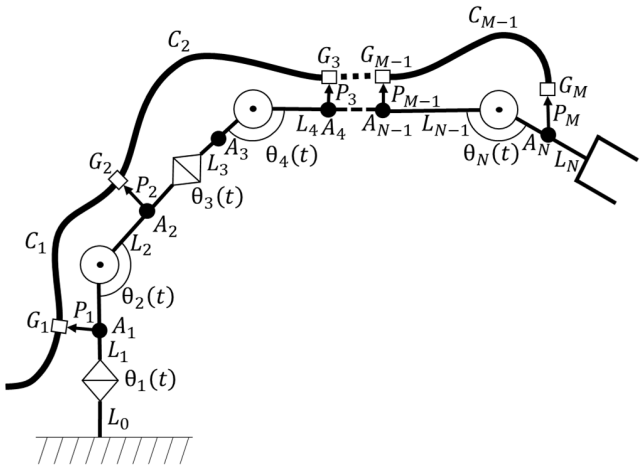

FIGURE 2. Schematic of an N-link robot arm with the cable and guide configuration.

introducing the procedure shown in Fig. 1. Here, the proposed method extracts critical poses, i.e., several static poses of the robot that are prone to applying stress to the cable, from the joint angle time series of the motion path and then performs attachment and motion tests. The definitions of the symbols in Fig. 1 are explained in the later subsections.

In the attachment test, the PV candidates that satisfy the constraints are selected by simulating the attachment of a cable to a static critical pose. A CSAT is used to remove the PV candidates that do not satisfy the adjacency conditions from the PV candidates that satisfy the constraints in the preceding cable segment.

In the motion test, the cable shape is simulated for the dynamic robot motion using the entire cable PV (ECPV), which is a combination of PV candidates selected in the attachment test, to determine the optimal combination of PVs that provides the shortest cable path satisfying the constraints.

The computational load for verifying each candidate PV in the attachment test is smaller than that for the motion test. The number of PV candidates to be validated in the motion test can be decreased by carefully selecting as few PV candidates as feasible in the attachment test. The proposed computational framework, in which the attachment and motion tests are coupled in series, is henceforth referred to as the cascade structure for cable path optimization.

The modeling of the robot arm and cables is described in Subsection II-A, the critical poses are mathematically defined in Subsection II-B, the attachment test is presented in Subsection II-C, and the motion test is presented in Subsection II-D.

A. ROBOT ARM AND CABLE MODELING

Fig.2 shows a robot arm, that consists of $N + 1$ links L_n ($n = 0, \ldots, N$) connected by N joints. Link L_0 is fixed to the robot platform. The n-th joint angle, which represents the relative angle of link L_n to link L_{n-1}, is expressed in terms of $\theta_n(t)$ as a function of time t. Let coordinate system, Σ_{L_0}, be the absolute coordinate system with the origin at the base point of link L_0, and the coordinate system, Σ_{L_n}, be the local coordinate system of L_n with the origin at the base point of L_n. Each L_n possesses a pair of screw holes for device attachment, indicated by black dots, and the configuration of the pair of screw holes in Σ_{L_n} is represented by A_n. The configuration of L_n at t is represented as a nonlinear function of the joint angle $\Theta(t) = [\theta_1(t), \theta_2(t), \ldots, \theta_N(t)]^T$.

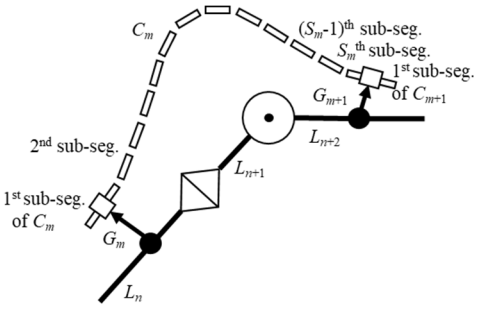

FIGURE 3. Subsegments in cable segment C_m.

As it is not possible to place guides on all links due to the specifications of the robot arm, the cables may be connected between adjacent links and between links that are one or more links apart. In this study, we assume that the cable guide G_m ($m = 1, \ldots, M$) is attached to L_n ($n = 1, \ldots, N$). Here, the relation between m and n is expressed as $n = f_{GuideToLink}(m)$ using the mapping function $f_{GuideToLink}(m)$. The configuration of G_m in Σ_{L_n} is given by the relative configuration P_m with respect to A_n of the pair of screw holes. Therefore, the configuration of G_m in Σ_{L_0} is a function of joint angles $[\theta_1(t), \theta_2(t), \ldots, \theta_n(t)]^T$, A_n, and P_m. The entire cable can be modeled as a set of cable segments C_m ($m = 1, \ldots, M-1$) [23]. The tip of C_m is attached to G_m and the end is attached to guide G_{m+1}.

A cable geometry model is used on the basis of multiple rigid subsegments of a constant physical size and a virtual mass-spring joint [10]–[41]. The virtual joint with six degrees of freedom constrains two adjacent subsegments.

As shown in Fig. 3, C_m traversing two joints connects L_n and L_{n+2} via G_m and G_{m+1}, which are composed of S_m subsegments with a fixed-length l_{ss} and virtual joints. Here, the relation between the indexes of the guide and link is expressed as $n = f_{GuideToLink}(m')|_{m'=m}$ and $n + 2 = f_{GuideToLink}(m')|_{m'=m+1}$ using the mapping function $f_{GuideToLink}$, where m and n are fixed values.

Thus, the length of C_m, l_{c_m}, is expressed as $S_m \times l_{ss}$. The first subsegment of C_m is connected to G_m, and the S_m-th subsegment is connected to the first subsegment of the next cable segment. The shape of C_m is calculated on the basis of the configuration of S_m subsegments.

B. CRITICAL POSES

Critical poses are robot poses that are prone to applying stress to the cable with impulse, stretching, bending, and other movements. Various critical poses are extracted for each

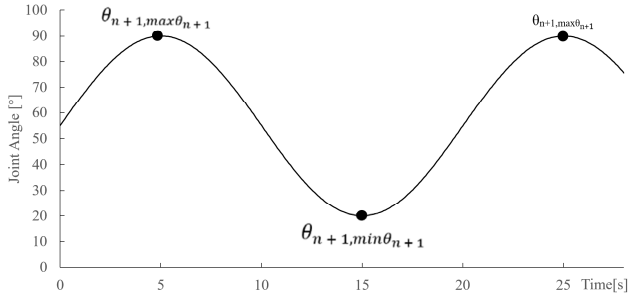

FIGURE 4. Joint angles and critical poses when one joint is present between the guides.

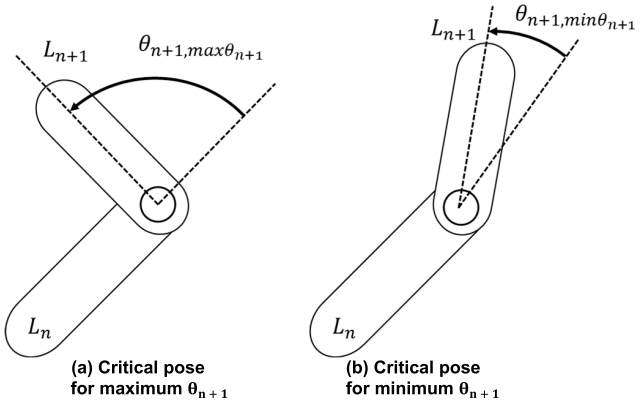

FIGURE 5. Critical robot poses with one joint between the links.

cable segment based on the robot motion. A critical pose is defined in terms of the joint angle with a global extreme value. In critical poses, satisfying the aforementioned stress constraint is difficult. Herein, it is assumed that if a cable path can satisfy the stress constraint in all critical poses, the cable can also satisfy the stress constraint in other motion poses.

Moreover, it is assumed that the cable stress generated in the static critical pose will be reproduced as the cable stress that damages the cable in the dynamic motion. Therefore, using the aforementioned framework of the cascade structure for cable path optimization, PVs that did not satisfy all the constraints in any critical pose in the attachment test from the set of PV candidates for the motion test are excluded.

The joint-angle time series $\Theta(t)$, which represents the robot motion, is generally obtained by applying a path-optimization method to a list of waypoint poses specified by the operator. The critical poses are extracted from $\Theta(t)$ using an order-dependent combination of the global extreme angles of the joints between the two guides. The scenarios for one and two joints between the guides are explained in the following parts; the scenarios for more joints can be explained by increasing the number of combinations.

1) CRITICAL POSES: ONE JOINT IS PRESENT BETWEEN THE GUIDES

The mathematical definition of critical poses is provided where one joint is present between the guides G_m and G_{m+1} to which C_m is attached. A set of critical pose tuples, Θ_m, comprises up to two tuples corresponding to the maximum and minimum values of the joint angle $\theta_{n+1}(t)$:

$$T_{max\theta_{n+1}} = \theta_{n+1}(t) \tag{1}$$
$$\theta_{n+1,max\theta_{n+1}} = = \theta_{n+1}(t)\, for\, t \in T_{max\theta_{n+1}} \tag{2}$$
$$T_{min\theta_{n+1}} = \theta_{n+1}(t) \tag{3}$$
$$\theta_{n+1,min\theta_{n+1}} = \theta_{n+1}(t)\, for\, t \in T_{min\theta_{n+1}} \tag{4}$$
$$\Theta_m = \{(\theta_{n+1,max\theta_{n+1}}), (\theta_{n+1,min\theta_{n+1}})\}, \tag{5}$$

As an example, Fig. 4 shows the joint angle and critical poses when one joint is present between the guides to which the cable is attached. For simplicity, the joint angles can be expressed using trigonometric functions. Here, the joint angle, θ_{n+1}, has the critical pose tuples $(\theta_{n+1,max\theta_{n+1}})$ and $(\theta_{n+1,min\theta_{n+1}})$ corresponding to the maximum values at 5 and 25 s (refer to (2)) and the minimum value at 15 s (refer to (4)), respectively. For reference, the respective critical poses are shown in Fig. 5.

Generally, the cable segment is stretched the most in the poses where the bending joint angle $\theta_{n+1} = 0$. However, such poses are likely to be eliminated as singular poses during trajectory planning. Thus, they are not adopted as candidates for critical poses in this study. However, they can be adopted as additional candidates.

In the case where two joints are present between the guides to which the cables are attached, the joint angles θ_{n+1} and θ_{n+2}, which are prone to applying stress to C_m that connects L_n and L_{n+2}, are determined by the maximum or minimum combination of each joint angle.

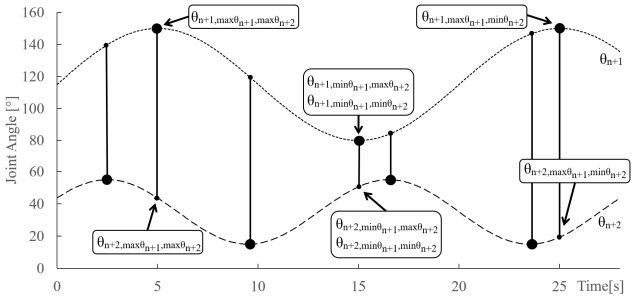

FIGURE 6. Joint angles and critical poses when two joints are present between the guides.

2) CRITICAL POSES: TWO JOINTS ARE PRESENT BETWEEN THE GUIDES

The mathematical definition of critical poses is provided where two joints are present between the guides G_m and G_{m+1} to which C_m is attached. Further, a set of critical pose tuples, Θ_m, comprises up to eight tuples corresponding to the order-dependent combinations of the maximum and minimum of two joint angles$\theta_{n+1}(t)$ and $\theta_{n+2}(t)$. Each tuple has two elements corresponding to respective joint angles:

$$T_{max\theta_{n+1}} = \theta_{n+1}(t) \tag{6}$$

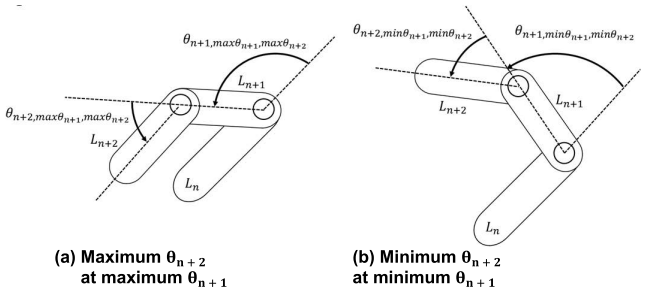

(a) Maximum θ_{n+2} at maximum θ_{n+1} (b) Minimum θ_{n+2} at minimum θ_{n+1}

FIGURE 7. Critical robot poses for two degrees of freedom between links.

$$T_{max\theta_{n+1},max\theta_{n+2}} = \theta_{n+2}(t) \tag{7}$$

$$\theta_{n+1,max\theta_{n+1},max\theta_{n+2}} = \theta_{n+1}(t)\, for\, t \in T_{max\theta_{n+1},max\theta_{n+2}} \tag{8}$$

$$\theta_{n+2,max\theta_{n+1},max\theta_{n+2}} = \theta_{n+2}(t)\, for\, t \in T_{max\theta_{n+1},max\theta_{n+2}} \tag{9}$$

$$\begin{aligned}\Theta_m = \{&(\theta_{n+1,max\theta_{n+1},max\theta_{n+2}}, \theta_{n+2,max\theta_{n+1},max\theta_{n+2}}),\\ &(\theta_{n+1,max\theta_{n+1},min\theta_{n+2}}, \theta_{n+2,max\theta_{n+1},min\theta_{n+2}}),\\ &(\theta_{n+1,min\theta_{n+1},min\theta_{n+2}}, \theta_{n+2,min\theta_{n+1},min\theta_{n+2}}),\\ &(\theta_{n+1,min\theta_{n+1},max\theta_{n+2}}, \theta_{n+2,min\theta_{n+1},max\theta_{n+2}}),\\ &(\theta_{n+1,max\theta_{n+2},max\theta_{n+1}}, \theta_{n+2,max\theta_{n+2},max\theta_{n+1}}),\\ &(\theta_{n+1,max\theta_{n+2},min\theta_{n+1}}, \theta_{n+2,max\theta_{n+2},min\theta_{n+1}}),\\ &(\theta_{n+1,min\theta_{n+2},min\theta_{n+1}}, \theta_{n+2,min\theta_{n+2},min\theta_{n+1}}),\\ &(\theta_{n+1,min\theta_{n+2},max\theta_{n+1}}, \theta_{n+2,min\theta_{n+2},max\theta_{n+1}})\}.\end{aligned} \tag{10}$$

The second and subsequent tuples in the right side of (10) are defined in the same way as the first tuple. During the actual robot motion, the number of critical pose tuples may be smaller owing to the overlap of these critical poses. For example, if $T_{max\theta_{n+1}} \cap T_{max\theta_{n+2}} \neq \emptyset$, then $\theta_{n+1,max\theta_{n+1},max\theta_{n+2}} = \theta_{n+1,max\theta_{n+2},max\theta_{n+1}}$ and $\theta_{n+2,max\theta_{n+1},max\theta_{n+2}} = \theta_{n+2,max\theta_{n+2},max\theta_{n+1}}$, yielding $(\theta_{n+1,max\theta_{n+1},max\theta_{n+2}}, \theta_{n+2,max\theta_{n+1},max\theta_{n+2}}) = (\theta_{n+1,max\theta_{n+2},max\theta_{n+1}}, \theta_{n+2,max\theta_{n+2},max\theta_{n+1}})$.

Fig. 6 shows the joint angle and critical poses when two joints are present between the guides. The dotted and dashed lines represent θ_{n+1} and θ_{n+2}, respectively. For simplicity, the joint angles can be expressed using trigonometric functions. First, we focus on 5 and 25 s where θ_{n+1} achieves the maximum values, and θ_{n+2} achieves the maximum value at 5 s and a minimum value at 25 s. Thus, critical pose tuples $(\theta_{n+1,max\theta_{n+1},max\theta_{n+2}}, \theta_{n+2,max\theta_{n+1},max\theta_{n+2}})$ and $(\theta_{n+1,max\theta_{n+1},min\theta_{n+2}}, \theta_{n+2,max\theta_{n+1},min\theta_{n+2}})$ are obtained at 5 and 25 s, respectively. Next, we focus on the case where θ_{n+1} reaches the minimum value; as θ_{n+1} achieves the minimum value only in 15 s, the critical pose at this time corresponds to both tuples $(\theta_{n+1,min\theta_{n+1},max\theta_{n+2}}, \theta_{n+2,min\theta_{n+1},max\theta_{n+2}})$ and $(\theta_{n+1,min\theta_{n+1},min\theta_{n+2}}, \theta_{n+2,min\theta_{n+1},min\theta_{n+2}})$. Therefore, there are three critical poses based on the global extremes of θ_{n+1}, and there are four critical poses based on the global extremes of θ_{n+2}. In total, seven critical poses are extracted from the two joint angles shown in Fig. 6. For reference, the critical pose tuples $(\theta_{n+1,max\theta_{n+1},max\theta_{n+2}}, \theta_{n+2,max\theta_{n+1},max\theta_{n+2}})$ and $(\theta_{n+1,min\theta_{n+1},min\theta_{n+2}}, \theta_{n+2,min\theta_{n+1},min\theta_{n+2}})$ are shown in Fig. 7.

Generally, Θ_m comprises $K(1 \leq K \leq 2^{i+1})$ pose tuples, where i represents the number of joints between the guides and each tuple comprises i elements. Each pose tuple included in Θ_m is denoted as the j-th critical pose ($j = 1, 2, \ldots, K$).

C. ATTACHMENT TEST

In the attachment test, the PV candidates that satisfy all the constraints are selected by simulating the attachment of a cable to a static critical pose. The attachment test procedure is depicted in the upper portion of Fig. 1. For the CSAT, the PV candidates that satisfy the constraints of each cable segment are selected in each attachment test module; then, the PV candidates that satisfy the constraints of all cable segments are selected.

The PV of a C_m comprises S_m (number of subsegments of C_m), P_m (configuration of G_m), and P_{m+1} (configuration of G_{m+1}). The PV candidate set $D_{0,m}$, which is generated on the basis of the combination of all these parameters, is defined as follows.

$$\begin{aligned}D_{0,m} = \{&(S_{m,i,m}, P_{m,j,m}, P_m + 1, jm + 1)|\\ &1 \leq i_m \leq I_m, 1 \leq j_m \leq J_m, 1 \leq j_{m+1} \leq J_{m+1},\\ &1 \leq m < M,\end{aligned} \tag{11}$$

where $\{S_{m,i_m}|1 \leq i_m \leq I_m\}$ denotes the candidate set of the number of subsegments in C_m that connects $L_{f_{GuideToLink}(m)}$ and $L_{f_{GuideToLink}(m+1)}$ and I_m denotes the candidate number of subsegments. The number of subsegments in the candidate set, S_{m,i_m}, is prepared as an arithmetic series of constant interval ΔS. Furthermore, $\{P_{m,j_m} P_{m,jm}|1 \leq J_m\}$ denotes the candidate set of configurations of G_m fixed to $L_{f_{GuideToLink}(m)}$and J_m represents the number of candidate guide configurations. $\{P_{m+1,j_{m+1}}[ERR : md : MbegChr = 0 \times 007C, MendChr = 0 \times 007D, nParams = 1]$ indicates the candidate set of configurations for G_{m+1} fixed to $L_{f_{GuideToLink}(m+1)}$.

As shown in Fig. 1, the attachment test consists of attachment test modules for individual cable segments and adjacency condition checks between adjacent cable segments. This structure aims to efficiently reduce the number of PV candidates; it is referred to as the CSAT.

Subsequently, three stress constraints on impulse, stretch, and bending [23] are considered for all poses in the critical pose set Θ_m. The PV set $D_{1,m}$ that satisfies these stress constraints is obtained as follows:

$$\begin{aligned}D_{1,m} = \{&(S_{m,i,m}, P_{m,j,m}, P_m + 1, jm + 1)|\\ Impulse_{th} \geq\ &Impulse_{(S_{m,i_m},P_{m,j_m},P_{m+1,j_{m+1}})}(\theta),\\ Stretch_{th} \geq\ &Stretch_{(S_{m,i_m},P_{m,j_m},P_{m+1,j_{m+1}})}(\theta),\\ Curvature_{th} \leq\ &Curvature_{(S_{m,i_m},P_{m,j_m},P_{m+1,j_{m+1}})}(\theta),\\ &for \forall\theta \in \Theta_m\}\end{aligned} \tag{12}$$

where $Impulse_{(S_{m,i_m},P_{m,j_m},P_{m+1,j_{m+1}})}(\theta)$ represents the maximum impulse received by each subsegment of C_m, when the joint angle is set to Θ_m. Similarly, $Stretch_{(S_{m,i_m},P_{m,j_m},P_{m+1,j_{m+1}})}(\theta)$ and $Curvature_{(S_{m,i_m},P_{m,j_m},P_{m+1,j_{m+1}})}(\theta)$are the maximum stretch and minimum radius of the curvature of the subsegments, respectively. The stress constraints described in (12) impose the following constrains on the cable [20].

Constraint 1: The impulse received by the cable when contacting the robot arm or peripheral objects is less than the threshold $Impulse_{th}$.

Constraint 2: The stretch rate of the distance between adjacent subsegments of the cable to a predefined distance is less than the threshold $Stretch_{th}$.

Constraint 3: The minimum cable curvature radius is more than the threshold $Curvature_{th}$ as determined by the cable material.

A robustness constraint on the length of C_m(the number of subsegments) is introduced so that the PVs satisfy the aforementioned stress constraints even if the number of subsegments increases or decreases within a predetermined robustness R [23]. Let l_R be the variation in the segment length corresponding to the robustness, $\mathrm{R} = l_R/(\Delta S \times l_{ss})$. A set of R-neighbor PVs associated with the index i_m in $\left(S_{m,i_m}, P_{m,j_m}, P_{m+1,j_{m+1}}\right)$ is defined as follows:

$$\begin{aligned} &D_{neighbor,(S_{m,i_m},P_{m,j_m},P_{m+1,j_{m+1}})} \\ &\quad = \left\{(S_{m,i'_m}, P_{m,j_m}, P_{m+1,j_{m+1}}) \middle|\ i_m \right. \\ &\qquad \left. - R \le i'_m \le i_m + R,\ 1 \le i'_m \le I_m \right\}. \end{aligned} \tag{13}$$

Based on $D_{neighbor}$ and $D_{1,m}$, the PV set $D_{2,m}$ that satisfies the robustness constraint is defined as follows:

$$\begin{aligned} D_{2,m} = \big\{ &\left(S_{m,i_m}, P_{m,j_m}, P_{m+1,j_{m+1}}\right) | \\ &\times D_{neighbor,(S_{m,i_m},P_{m,j_m},P_{m+1,j_{m+1}})} \subset D_{1,m}, \\ &1 \le i_m - R\ , i_m + R \le I_m \big\}. \end{aligned} \tag{14}$$

Next, the cable segment adjacency condition check is discussed for the CSAT (Fig. 1). For $2 \le m$, $D'_{0,m}$ is used instead of $D_{0,m}$ as the input for the attachment test module. Here, $D'_{0,m}$ is generated as a subset of $D_{0,m}$ by checking the adjacency condition using the already obtained $D_{2,m-1}$, as shown in (15). Notably, the attachment test procedure is written in such a way that PVs are verified in the order of subsegment cables with low index m. However, by performing PV reduction in the order of subsegment cables with a small number of PV candidates, the total computation time of the attachment test can be reduced.

$$\begin{aligned} D'_{0,m} = \big\{ &S_{m,i_m}, P_{m,j_m}, P_{m+1,j_{m+1}} \big| \\ &\left(S_{m-1,i_{m-1}}, P_{m-1,j_{m-1}}, P_{m,j_m}\right) \in D_{2,m-1}, \\ &\left(S_{m,i_m}, P_{m,j_m}, P_{m+1,j_{m+1}}\right) \in D_{0,m} \big\} \end{aligned} \tag{15}$$

Next, the procedure to combine the PVs in $\{D_{2,m}|1 \le m < M$ obtained using the attachment test is described for all cable segments $\{C_m|1 \le m < M$ to determine the global optimal PV that minimizes the total number of subsegments in the entire cable. The adjacency condition check is applied throughout the cable, in which the adjacent cables must share the same configuration of the guides that connect them [23]. The PV set D_3 that satisfies the adjacency condition can be expressed as follows:

$$\begin{aligned} &D_3 \\ &\quad = \big\{ S_{1,i_1}, \ldots, S_{m,i_m}, \ldots, S_{M-1,i_{M-1}}, \\ &\qquad P_{1,j_1}, \ldots, P_{m,j_m}, \ldots, P_{M,j_M} \big| \\ &\qquad \times \left(S_{m,i_m}, P_{m,j_m}, P_{m+1,j_{m+1}}\right) \in D_{2,m},\ 1 \le m < M \big\} \end{aligned} \tag{16}$$

Here, the elements in D_3 are denoted as ECPVs. If $D_3 = \emptyset$, then there is no cable path for the given robot motion.

Algorithm 1 Motion test algorithm

Input: D_3, $\Theta(t)$
Output: d^*

$D'_3 \leftarrow D_3$
while $D'_3 \neq \emptyset$
$\hat{d} = \arg\min_{d} \sum_{m=1}^{M-1} S_{m,i_m}$ $\quad d \epsilon D'_3$
if in parallel for m
  $Impulse_{th} \ge \max_{0 \le t \le T} Impulse_m^{\hat{d}}(\Theta(t))$
  and $Stretch_{th} \ge \max_{0 \le t \le T} Stretch_m^{\hat{d}}(\Theta(t))$
  and $Curvature_{th} \le \max_{0 \le t \le T} Curvature_m^{\hat{d}}(\Theta(t))$
then
  $d^* \leftarrow \hat{d}$
  break
else
  $D'_3 \leftarrow D'_3 \setminus \{\hat{d}\}$
end while

D. MOTION TEST

In the motion test, the cable geometry is simulated on the basis of the dynamic robot motion using the ECPVs selected during the attachment test, where the optimal ECPV that provides the shortest cable path and satisfies the constraints is selected. The motion test procedure is depicted in the lower portion of Fig. 1.

First, D_3 is copied into the set D'_3. Next, the ECPV with the shortest entire cable length in D'_3 is selected and denoted as $\hat{d}$. A motion simulation is parallelly performed on $\hat{d}$ for each cable segment $C_m(1 \le m < M)$ to determine whether the stress and robustness constraints are satisfied. If both the constraints are satisfied, the process is terminated and $\hat{d}$ is adopted as the optimal solution of the cable path, d^*; otherwise, the current $\hat{d}$ is removed from D'_3 and the motion test is performed using the ECPV candidates with the shortest total cable length as the new $\hat{d}$. If D'_3 becomes empty, all combinations of PVs in the candidate set $D_{0,m}(1 \le m < M)$ do not satisfy the design requirements. This process is described in Algorithm 1, where $Impulse_m^{\hat{d}}(\Theta(t))$ is the maximum impulse received by all the subsegments on C_m

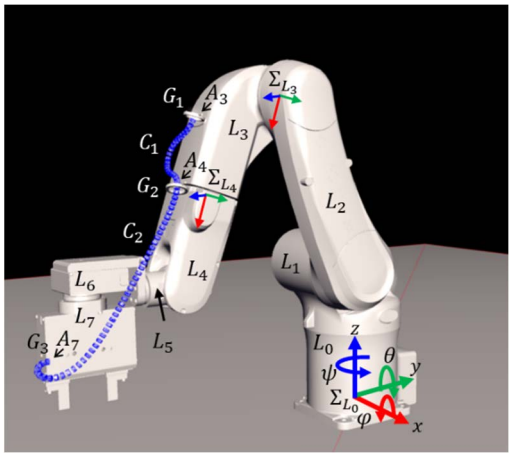

FIGURE 8. Six-axis vertically articulated robot arm equipped with a cable.

at the time t. $Stretch_m^{\hat{d}}(\Theta(t))$ and $Curvature_m^{\hat{d}}(\Theta(t))$ are the maximum stretch and minimum curvature, respectively.

III. SIMULATION

The proposed method was used for automatically designing cable paths in pick-and-place motions, and the required computation time was compared with that of the conventional method [23]. The simulation was performed using a six-axis articulated robot (Omron Viper 850 [42]) with an electric gripper (SMC LEHF32EK2-32 [43]). A cable (SMC LE-CP-3 [44]; diameter: 8 mm and weight: 260 g/m) used to transmit power and control signals to the electric gripper was the target of the cable geometry simulation.

For the physical simulation of the cable geometry, the mass–spring model in PhysX SDK 4.0 [14] was used, and the rigid segments were connected via virtual joints with six degrees of freedom. The bending and torsion spring constants were set to 5.1×10^{-2} and 1.5 Nm/rad, respectively, using a measurement method [23]. The damping coefficient was set to 1.0×10^2Ns/m. The specifications of the computer are as follows: OS: Windows 10 Professional, CPU: Intel Core i9-7980XE 2.6 GHz, RAM: 16 GB, GPU: NVIDIA GeForce RTX 2080.

In this section, the setting of the parameters included in the stress constraints of the cable geometry (refer to (12)) during cable simulation is described. To avoid collisions with the surrounding objects, $Impulse_{th}$ was set to 0. Considering physical stress, $Stretch_{th}$can be set to 100%. However, considering the oscillation of the cable geometry, $Stretch_{th}$ was set to 102%. $Curvature_{th}$ was set to 48 mm, which is six times the diameter of the test cable.

A. PARAMETERIZATION OF GUIDES AND CABLES

The parameters for the number of subsegments of the cable segment and the configuration of the guide to be optimized were defined. In addition to the relevant coordinate systems, Fig. 8 shows the links, configuration of the pair of screw holes for device attachment, the guides and cables. The robot arm comprised L_1–L_6; the gripper section L_7 was fixed to L_6. The origin of the absolute coordinate system, Σ_{L_0}, was the base of the robot arm, and the origin of Σ_{L_n} was the base of $L_n (1 \leq n \leq 7)$. Guides G_1, G_2, and G_3 were attached to L_3, L_4, and L_7, respectively. As described in Subsection III-A, the configuration P_m of G_m is specified as a relative configuration with respect to configuration of the pair of the screw holes, A_n, in Σ_{L_n}. Here, the mapping relations using the function $f_{GuideToLink}$ are expressed as $1 \rightarrow 3$, $2 \rightarrow 4$, and$3 \rightarrow 7$. Cable C_1 connected G_1 and G_2, while C_2 connected $G_2$and G_3.

The PV for C_1 includes the number of subsegments, S_1, and the configurations, P_1 of $G_1$and P_2 of G_2. Similarly, the PV for C_2 includes the number of subsegments, S_2, and the configurations, P_2 of G_2 and P_3 of G_3. Usually, the external cable connection to L_3 is suspended from the ceiling or girders; however, this cable path design is not considered for the optimization in this study. Therefore, the parameters to be optimized wereS_1, S_2, P_1, P_2, and P_3.

The minimum value of S_1 was determined based on the distance between the screw holes of L_3 and L_4 in the initial pose. Similarly, the distance between the screw holes of $L_4$and L_7 was used to estimate the minimum value of S_2. The maximum values of S_1 and S_2 were calculated by adding appropriate values to the corresponding minimum values in terms of the range of expected solutions and computation time. In particular, the values of $C_1 = 150$–250 mm, $C_2 = 400$–520 mm, and $l_{ss} = 10$ mm were set. The step width of the cable segment length for the optimization was set to 10 mm ($\Delta S = 1$). Thus, the candidates for S_1 and S_2 are$\left(S_{1,1}, S_{1,2}, \cdots, S_{1,11}\right) = (15, 16, \cdots, 25)$ and $\left(S_{2,1}, S_{2,2}, \cdots, S_{2,13}\right) = (40, 41, \cdots, 52)$, respectively. Here, the numbers of candidates are $I_1 = 11$ and $I_2 = 13$. A 10-mm unit subsegment comprised a cylinder of 5-mm length and 8-mm diameter as well as a 5-mm void (virtual joint). The robustness range parameter R was set to $2 (= \frac{l_R}{\Delta S \times l_{ss}} = \frac{20\text{mm}}{1 \times 10\text{mm}})$ to allow a 20-mm variation in l_R for C_1 and C_2.

The configuration P_m of G_m comprises the position (x, y, z) and orientation (φ, θ, ψ) (units: millimeters and degrees, respectively). Here, φ is the twisting angle of the cable, which was fixed at 0° because twisting the cable before attaching it to the guide would decrease its lifetime. The candidate set of positions for the configuration P_1 of G_1 is $\{(x, y, z) | x = 0, y = -40, 0, 40, z = 0, 20\}$ and that of orientations for P_1 is $(\varphi, \theta, \psi) | \varphi = 0, \theta = 0, \psi = -90, -45, 0, 45, 90$, affording $J_1 = 30$. Furthermore, the candidate set of positions for P_2 is $\{(x, y, z) | x = 0, 50, y = -60, 0, 60, z = 0, 20\}$ and that of the orientations for P_2 is $\{(\varphi, \theta, \psi) | \varphi = 0, \theta = 0, \psi = -90, -45, 0, 45, 90\}$, affording $J_2 = 60$.

B. ROBOT ARM MOTIONS

Pick-and-place motions are frequently performed in industrial robot applications. Herein, the cable path optimization for two pick-and-place motions was investigated. These motions are defined as a series of robot poses with respect

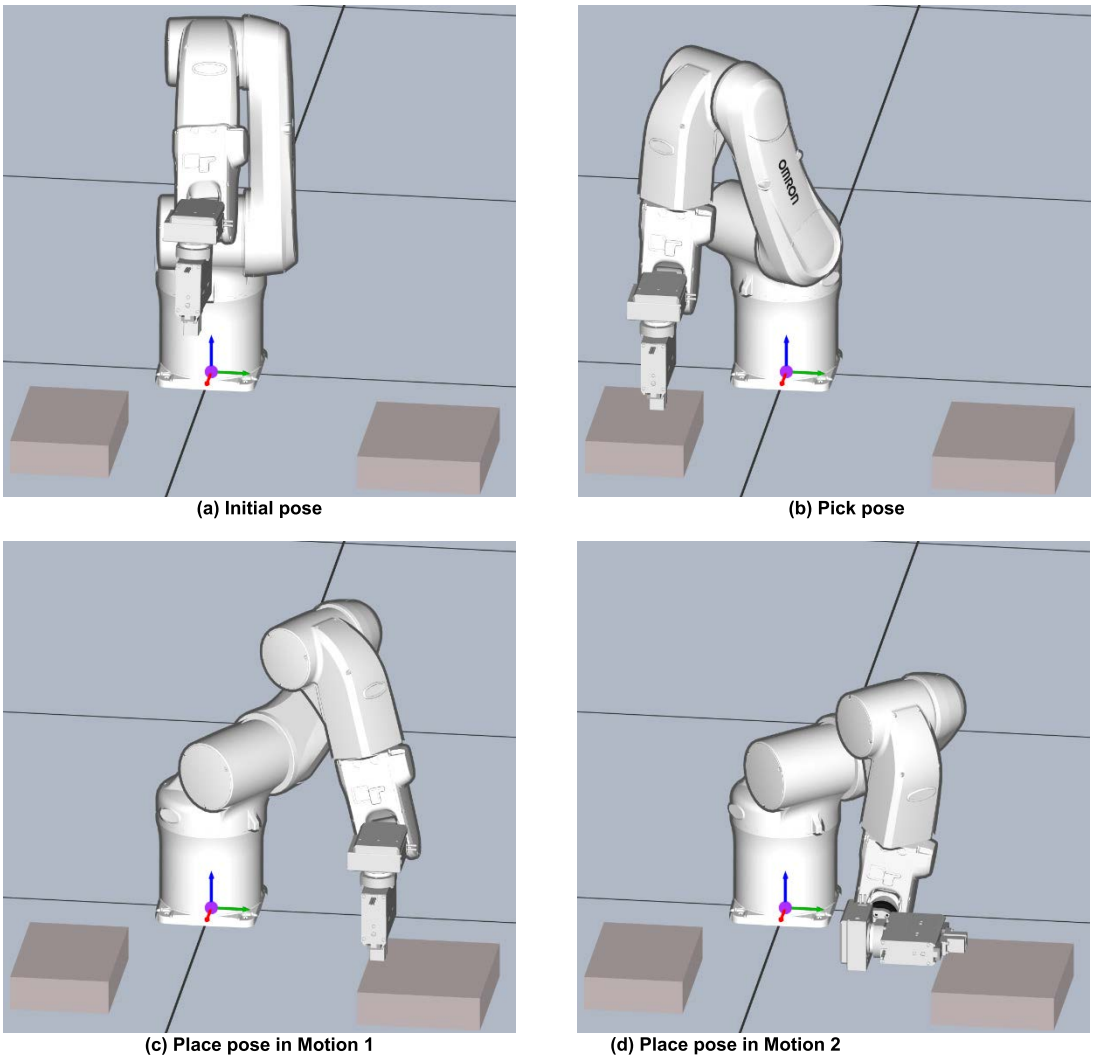

FIGURE 9. Poses in pick-and-place motions of the robot arm.

to Σ_{L_0}. The initial pose of the robot arm is shown in Fig. 9(a). First, the robot arm picked an object at $(x, y, z) = (500, 0, 170)$ mm and $(\varphi, \theta, \psi) = (0, 90, -90)°$ (Fig. 9(b)). Then, the robot arm placed the object. The configuration of the placed object varies with each motion. The place configuration was $(x, y, z) = (350, 240, 280)$mm and $(\varphi, \theta, \psi) = (0, 90, -90)°$ (Fig. 9(c)). However, in Motion 2 (Fig. 9(d)), the place configuration was $(x, y, z) = (450, 240, 125)$mm and $(\varphi, \theta, \psi) = (0, 90, 0)°$. The joint-angle time series $\Theta(t)$ was generated using Omron Sysmac Studio [45], a robot programming environment, based on a script that detailed the transit points, velocities, and other factors related to the two pick-and-place motions. Finally, the $(\theta_1, \theta_2, \theta_3, \theta_4, \theta_5, \theta_6)$ of the initial, pick, and place poses in Motions 1 and 2 are shown in Table 1.

C. CRITICAL POSE EXTRACTION

In this section, the results of the extracted critical poses for the attachment test from Motions 1 and 2 are described. Based on the $\Theta(t)$ of each motion, the critical pose sets Θ_1 and Θ_2 of C_1 and C_2 were obtained using (5) and (10), respectively.

TABLE 1. Poses in Pick-and-Place Motions.

Pose	$(\theta_1, \theta_2, \theta_3, \theta_4, \theta_5, \theta_6)$
Initial pose	(6.4°, −104.6°, 240.3°, 9.3°, −52.1°, −97.0°)
Pick pose	(−36.5°, −68.5°, 243.2°, −36.7°, −85.7°, −86.8°)
Place pose in Motion 1	(56.0°, −56.6°, 219.2°, 57.2°, −80.4°, −104.5°)
Place pose in Motion 2	(33.3°, −33.6°, 217.4°, 32.8°, −93.4°, 2.1°)

First, Motion 1 is considered. Table 2 shows the joint angles of the Θ_1 of C_1, and Table 3 shows the joint angles of the Θ_2 of C_2. Θ_1 and Θ_2 contain two and four pose tuples (Fig. 10 and Fig. 11), respectively. As mentioned in Subsection III-B, C_2 connects L_4 and L_6; hence, there are two joints between G_2 and G_3. Therefore, Θ_2 may contain up to eight pose tuples. However, only four unique pose tuples were extracted owing to the overlapping of the original pose tuples.

TABLE 2. Critical Pose Θ_1 of C_1 for Motion 1.

Pose tuple	Θ_1	Order of critical pose
$(\theta_{4,max\theta_4})$	(−37.3°)	1st
$(\theta_{4,min\theta_4})$	(57.7°)	2nd

TABLE 3. Critical Pose Θ_2 of C_2 for Motion 1.

Pose tuple	Θ_2	Order of critical pose
$(\theta_{5,max\theta_5,max\theta_6}, \theta_{6,max\theta_5,max\theta_6})$	(−52.1°, −97.0°)	1st
$(\theta_{5,max\theta_5,min\theta_6}, \theta_{6,max\theta_5,min\theta_6})$	(−52.1°, −97.0°)	1st
$(\theta_{5,min\theta_5,min\theta_6}, \theta_{6,min\theta_5,min\theta_6})$	(−85.7°, −86.8°)	3rd
$(\theta_{5,min\theta_5,max\theta_6}, \theta_{6,min\theta_5,max\theta_6})$	(−85.7°, −86.8°)	3rd
$(\theta_{5,max\theta_6,max\theta_5}, \theta_{6,max\theta_6,max\theta_5})$	(−78.9°, −81.7°)	2nd
$(\theta_{5,max\theta_6,min\theta_5}, \theta_{6,max\theta_6,min\theta_5})$	(−78.9°, −81.7°)	2nd
$(\theta_{5,min\theta_6,min\theta_5}, \theta_{6,min\theta_6,min\theta_5})$	(−76.7°, −108.5°)	4th
$(\theta_{5,min\theta_6,max\theta_5}, \theta_{6,min\theta_6,max\theta_5})$	(−76.7°, −108.5°)	4th

Fig. 12 shows that $\theta_n(t)\,(4 \leq n \leq 6)$ is included in $\Theta(t)$. In this figure, the occurrence periods of the pick and place poses are indicated by double-sided arrows and the extraction times of Θ_1 and Θ_2 are indicated by black dots.

To discuss the two pose tuples of Θ_1 described in Table 2, the critical pose shapes presented in Fig. 10 and θ_4 (solid line) shown in Fig. 12 were observed. The critical pose shapes presented in Figs. 10(a) and 10(b) corresponded to the pick and place poses, respectively. However, the extraction time of the two critical poses on θ_4 in Fig. 12 revealed that the joint angle achieved an extreme value—not for the pick and place poses but for the approach and departure movements.

To discuss the four pose tuples of Θ_2 described in Table 3, the critical pose shapes presented in Fig. 11 as well as θ_5 (dotted line) and θ_6 (dashed line) shown in Fig. 12 were observed. The critical poses listed in Table 3 were indexed according to the order of the earliest time at which they were observed in Fig. 12. The first critical pose corresponded to the initial pose. The second and third critical poses were extracted around the pick pose, and the fourth critical pose was extracted around the place pose.

Considering the extracted critical poses of Motion 2, Tables 4 and 5 show the joint angles of Θ_1 and Θ_2 of C_1 and C_2, respectively. Both Θ_1 and Θ_2 contained two unique pose tuples (Figs. 13 and 14, respectively).

Fig. 15 shows that $\theta_n(t)\,(4 \leq n \leq 6)$ is included in $\Theta(t)$. The critical pose shapes presented in Fig. 13 and θ_4 (solid line) shown in Fig. 15 indicate that the first and second critical poses were extracted around the occurrence times of the initial and place poses, respectively. The extraction time of the second critical pose coincided with the beginning of the place pose process. Interestingly, no critical poses were extracted around the pick pose. This is because the values of θ_5 (dotted line) and θ_6 (dashed line) for the pick pose were no longer global extremes owing to the considerably larger θ_5 and smaller θ_6 values of the place pose for Motion2 than those for Motion 1.

TABLE 4. Critical Pose Θ_1 of C_1 for Motion 2.

Pose tuple	Θ_1	Order of critical pose
$(\theta_{4,max\theta_4})$	(−37.3°)	1st
$(\theta_{4,min\theta_4})$	(32.8°)	2nd

TABLE 5. Critical Pose Θ_2 of C_2 for Motion 2.

Pose tuple	Θ_2	Order of critical pose
$(\theta_{5,max\theta_5,max\theta_6}, \theta_{6,max\theta_5,max\theta_6})$	(−52.1°, −97.0°)	1st
$(\theta_{5,max\theta_5,min\theta_6}, \theta_{6,max\theta_5,min\theta_6})$	(−52.1°, −97.0°)	1st
$(\theta_{5,min\theta_5,min\theta_6}, \theta_{6,min\theta_5,min\theta_6})$	(−93.3°, 2.1°)	2nd
$(\theta_{5,min\theta_5,max\theta_6}, \theta_{6,min\theta_5,max\theta_6})$	(−93.3°, 2.1°)	2nd
$(\theta_{5,max\theta_6,max\theta_5}, \theta_{6,max\theta_6,max\theta_5})$	(−52.1°, −97.0°)	1st
$(\theta_{5,max\theta_6,min\theta_5}, \theta_{6,max\theta_6,min\theta_5})$	(−52.1°, −97.0°)	1st
$(\theta_{5,min\theta_6,min\theta_5}, \theta_{6,min\theta_6,min\theta_5})$	(−93.3°, 2.1°)	2nd
$(\theta_{5,min\theta_6,max\theta_5}, \theta_{6,min\theta_6,max\theta_5})$	(−93.3°, 2.1°)	2nd

TABLE 6. Computation Time for Each Module in the Cascade Structure in the Attachment Test.

Motion	Cascade structure	Cable		Time [min]		Total
		1st module	2nd module	1st module	2nd module	
1	CSAT1	C_1	C_2	78.8	7.3	86.0
	CSAT2	C_2	C_1	13.2	24.2	37.4
2	CSAT1	C_1	C_2	84.0	7.8	91.8
	CSAT2	C_2	C_1	12.9	20.5	33.4

D. ATTACHMENT TEST

As mentioned in Subsection III-A, fewer PV candidates were identified in the $D_{0,2}$ of C_2 (780) than those in the $D_{0,1}$ of C_1 (19,800). In the CSAT, completing the attachment test in an ascending order of the number of PV candidates for the cable subsegments may further reduce the computation time (Subsection II-C). Therefore, the relation between the order of the attachment test modules and the computation time is explored for each cable subsegment. Further, the computation time is obtained under the condition when the CSAT is not used.

When C_1 and C_2 were considered in the first and second modules, respectively (CSAT1), the set of ECPVs D_3 was determined using the module order (Fig. 1). However, when C_2 and C_1were considered in the first and second modules, respectively (CSAT2), the attachment test was first performed on the set of PV candidates $D_{0,2}$ associated with C_2 to obtain $D_{2,2}$ that satisfies the stress and robustness constraints. Then, the PV candidate set $D'_{0,1}$ was generated from $D_{2,2}$ and $D_{0,1}$ associated with C_1 using the adjacency condition check. The attachment test was performed on $D'_{0,1}$ to obtain $D_{2,1}$ that satisfies the constraints. Finally, the ECPV set D_3 was determined using $D_{2,1}$ and $D_{2,2}$.

The results of the attachment test for Motions 1 and 2 are discussed. Table 6 shows the computation time required to determine the PV and ECPV in $D_{2,1}$, $D_{2,2}$, and D_3 for C_1 and C_2. For Motions 1 and 2, the total computation time for CSAT2, which treats C_2 with few PVs in the first module, was considerably smaller than that for CSAT1. The computation

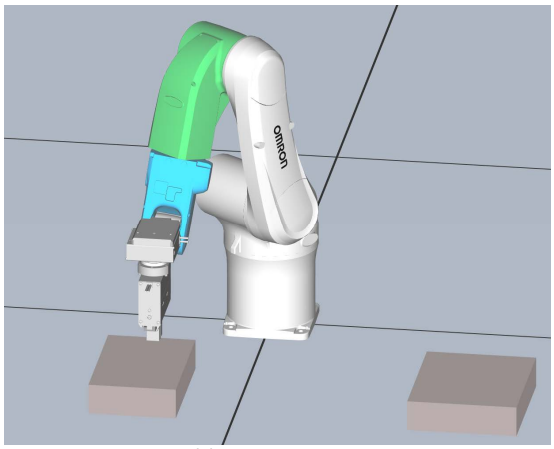

(a) 1st critical pose

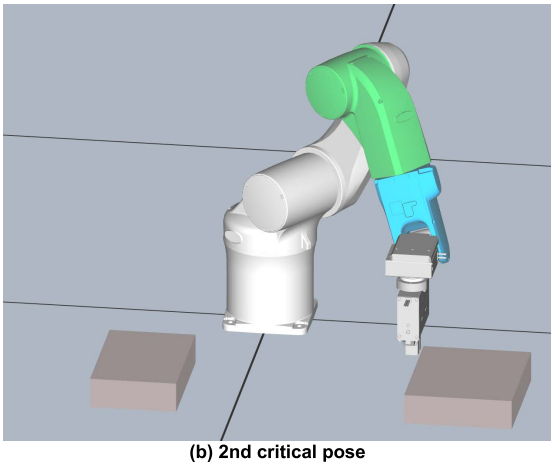

(b) 2nd critical pose

FIGURE 10. Critical pose Θ_1 of C_1 for Motion 1. Green: L_3 fixed with G_1; blue: L_4 fixed with G_2.

TABLE 7. Number of PVS of D_2 for Each Module and ECPVs OF D_3 in the Cascade Structure in the Attachment Test.

Motion	Cascade structure	Cable 1st module	Cable 2nd module	Number of PVs 1st module	Number of PVs 2nd module	Number of ECPVs
1	CSAT1	C_1	C_2	406 ($D_{2,1}$)	18 ($D_{2,2}$)	246 (D_3)
	CSAT2	C_2	C_1	57 ($D_{2,2}$)	109 ($D_{2,1}$)	246 (D_3)
2	CSAT1	C_1	C_2	697 ($D_{2,1}$)	10 ($D_{2,2}$)	131 (D_3)
	CSAT2	C_2	C_1	42 ($D_{2,2}$)	85 ($D_{2,1}$)	131 (D_3)

time in the second module for CSAT2 was slightly longer but that in the first module was considerably shorter, according to the computation time for each module. Notably, the total computation time without the CSAT was 92.0 min (78.8 + 13.2 min) and 96.9 min (84.0 + 12.9 min) for Motions 1 and 2, respectively. These findings suggest that using the CSAT reduces the computation time and treating cable segments with few PVs in the first module is recommended.

Fewer ECPVs were obtained in Motion 2 (131) than those in Motion 1 (246), indicating that designing a cable path suitable for Motion 2 is more challenging.

TABLE 8. ECPV Values in D_3 Obtained From Attachment Tests
(a) Motion 1.

(a) Motion 1

ECPV	$S_1 + S_2$	S_1	S_2	$P_1\ (x,y,z,\varphi,\theta,\psi)$	$P_2\ (x,y,z,\varphi,\theta,\psi)$
No.1	67	20	47	(0,40,0,0,0,0)	(0,60,20,0,0,0)
No.2	67	20	47	(0,40,20,0,0,0)	(0,60,20,0,0,0)
No.3	67	20	47	(0,40,0,0,0, −45)	(0,60,20,0,0,0)
No.4	68	20	48	(0,40,0,0,0,0)	(0,60,0,0,0,45)
No.5	68	20	48	(0,40,20,0,0,0)	(0,60,0,0,0,45)

(b) Motion 2

ECPV	$S_1 + S_2$	S_1	S_2	P_1	P_2
No.1	67	19	48	(0,40,0,0,0,0)	(0,60,0,0,0,45)
No.2	67	19	48	(0,40,0,0,0,45)	(0,60,0,0,0,45)
No.3	68	19	49	(0,40,0,0,0,0)	(0,60,20,0,0,45)
No.4	68	19	49	(0,40,0,0,0,45)	(0,60,20,0,0,45)
No.5	68	20	48	(0,40,20,0,0,0)	(0,60,0,0,0,45)

Table 7 shows the number of PVs and ECPVs in $D_{2,1}$ for C_1, $D_{2,2}$ for C_2, and D_3. In Motions 1 and 2, the number of PVs obtained in the first module of CSAT2 was considerably lower than that in the case of CSAT1, while the number of PVs in the second module was slightly higher. Notably, the total number of ECPVs in the cases of both CSATs was the same. Further, based on the results of a preliminary simulation, the numbers of ECPVs in the case of both CSATs were confirmed to be equal to that without CSAT.

The ECPVs included in the final set D_3 are shown in Table 8 in an ascending order of the entire cable length. The ECPVs obtained for each motion (TABLE 8 (a) and (b)) were compared. The sum of S_1 and S_2 of the ECPVs for both motions was similar. In particular, i) the ψ values in P_2 were 0° or 45° in Motion 1, whereas they were 45° in Motion 2. ii) the S_1 values for Motion 1 were slightly larger than those for Motion 2; and iii) the S_2 values for Motion 1 were smaller than those for Motion 2. These differences in the tendencies of ECPVs will be discussed later in Section IV.

The cable geometry simulation where $C_1$was connected to G_1 and G_2 is shown in Fig. 16. Initially, C_1 exhibited a linear shape along the −y direction of Σ_{L0}, and the position of the first subsegment was tied to the position of P_1. The configurations of the first and last subsegments were kinematically controlled over 100 steps such that their configurations eventually matched those of P_1 and P_2; alternatively, the geometries of other subsegments were physically simulated.

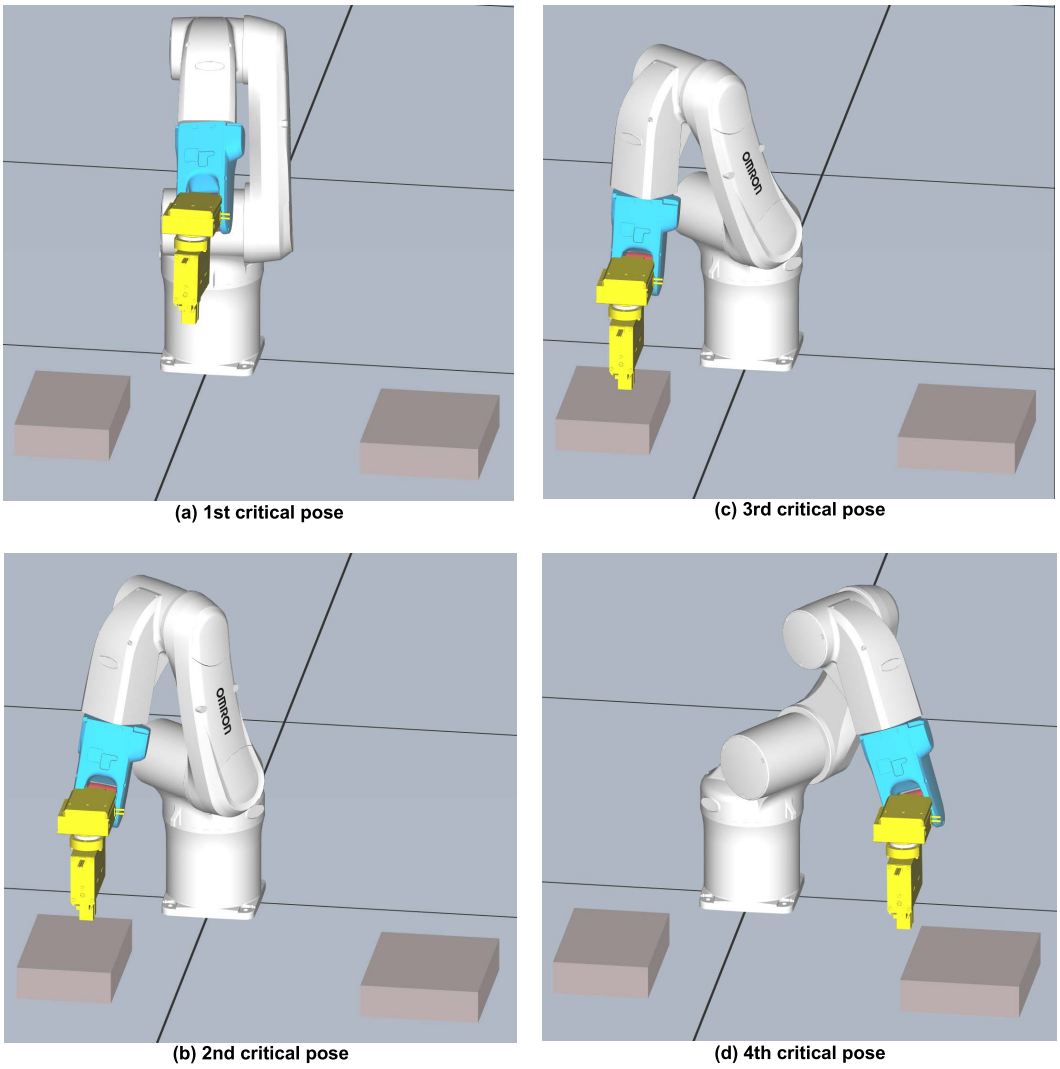

FIGURE 11. Critical pose Θ_2 of C_2 for motion 1. Yellow: L_7 fixed with G_3 and L_6; blue: L_4; red: L_5.

E. MOTION TEST

The optimal solution d^* as the shortest cable path satisfying the constraints was obtained by iteratively performing motion tests on the ECPVs in D_3 (Table 8) in the order of the increasing total cable length. To validate the reliability of the ECPVs obtained from the attachment test, the motion test was performed on all the ECPVs in D_3. The results showed that 84 of 246 ECPVs passed the motion test for Motion 1 and 75 of 131 ECPVs passed for Motion 2. Regarding Motion 1 presented in Table 8 (a), ECPV No.1 and No.2 violated the impulse constraint in the motion test and ECPV No.3 was selected as d^* for the optical cable path. Regarding Motion 2 presented in Table 8 (b), ECPV No.1 was selected as d^*.

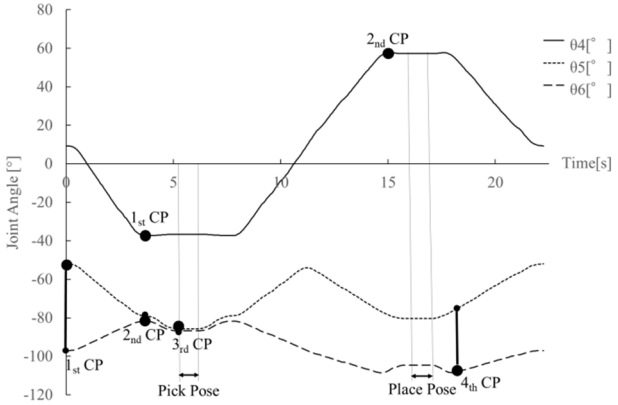

FIGURE 12. Joint angle time series with critical poses (CPs) for Motion 1.

F. DISCUSSION

1) CABLE GEOMETRIES IN ATTACHMENT AND MOTION SIMULATIONS

The cable geometries of the attachment and motion simulations in the critical poses of Motion 2 are shown in Figs. 17 and 18, respectively. The d^* for each motion was used to determine the optimal cable path. The cable segment geometries generated in both simulations were very similar

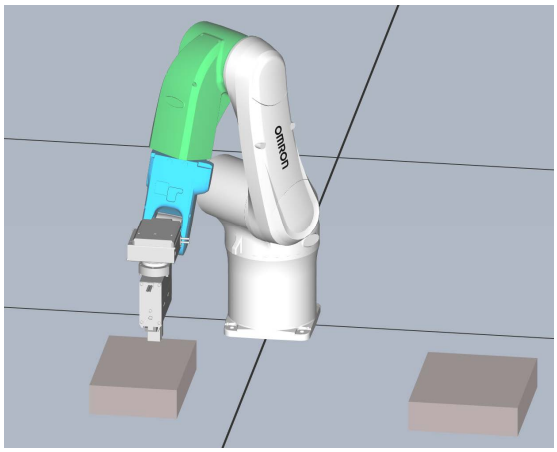

(a) 1st critical pose

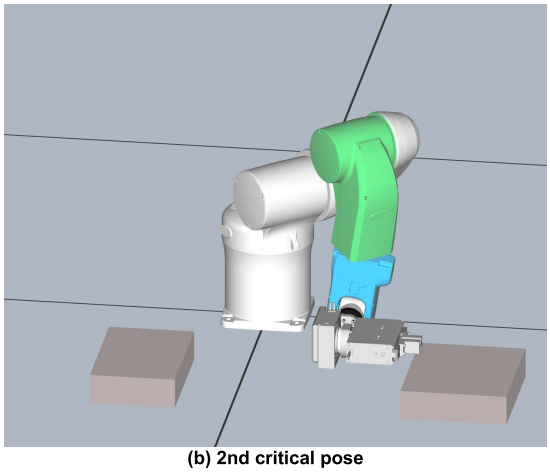

(b) 2nd critical pose

FIGURE 13. Critical pose Θ_1 for C_1 for Motion 2.

for both critical poses for C_1 (Figs. 17(a) and 18(a) as well as Figs. 17(b) and 18(b)) and both critical poses for C_2 (Figs. 17(c) and 18(c) as well as Figs. 17(d) and 18(d)). Similar results were obtained for Motion 1; however, these results were excluded from this manuscript for reasons of space.

2) COMPUTATION TIME COMPARISON

The times required to obtain d^* using the previous method [23] and the method proposed herein are compared in Table 9. First, the computation time obtained using the previous method is discussed, where motion tests were performed on all PVs in the candidate set $D_{0,1}$ of C_1 and $D_{0,2}$ of C_2 using a brute-force search. The computation time required for the 19,800 PVs in $D_{0,1}$ was considerably longer than that required for the 780 PVs in $D_{0,2}$. Since the computation for $D_{0,1}$ and $D_{0,2}$ were parallelized, the total time shown in this table is equal to the computation time for $D_{0,1}$.

Next, the computation time obtained using the proposed method is discussed, where the computation times for the motion test were 0.08 and 0.13 min per PV for Motions 1 and 2, respectively, resulting in a total estimated time of ∼27.5 and 42.9 h for all PVs, respectively. However, the total computation time was considerably less than the total estimated time (Table 9) because when the stress constraint failed, the simulation for each PV was halted.

Now, the total computation time of the attachment and motion tests using the proposed method is discussed. The computation times obtained in the attachment test are indicated as the total time for CSAT2 in Table 6. In the motion test per PV in an ECPV, five motion simulations were performed to determine whether the robustness constraint (R = 2) was satisfied. For Motion 2, the first ECPV candidate was selected; hence, the computation time in the motion test was the time required for five motion simulations, with the time required per motion simulation as 0.13 min. However, for Motion 1, the third ECPV candidate was selected, necessitating two extra motion simulations. Therefore, the computation time for the motion test was the time required for seven motion simulations, where the time required per motion simulation was 0.08 min.

As shown in Fig. 1, the motion simulations of C_1 and C_2 were executed parallelly. The total time is the sum of the time required for conducting the attachment and motion tests. The total times obtained using the proposed method were 3.2% and 2.2% of the total times obtained using the previous method for Motions 1 and 2, respectively.

The computation time was drastically reduced mainly by introducing the attachment test before the motion test. In the attachment test, the cable geometries with PV candidates were statically simulated for several critical poses, i.e., robot poses that are prone to applying stress to the cable and extracted from the robot motion. Conversely, in the motion test, the cable geometries with PV candidates were dynamically simulated for all the poses included in the robot motion. As described in Subsection II-B, the number of critical poses is limited by the degree of freedom of the robot link structure and the number of cable segments, while the number of all the poses in the robot motion is proportional to the sequence length of the robot motion. This insight is the reason why the computation time for the attachment test is considerably shorter than that for the motion test. In the method proposed herein, the PV candidates are considerably reduced in the attachment test with a shorter computation time per PV and the remaining PV candidates are inspected in the motion test with a longer computation time per PV according to the concept of the cascade structure for cable path optimization. Notably, if all PV candidates pass both the attachment and motion tests for a very simple robot motion, the total computation time obtained using the proposed method will be almost the same or slightly longer than that of our previous method where all PV candidates were inspected only in the motion test. However, the practical robot motions are complicated; thus, it is very rare for all PV candidates to pass both the tests. In addition, as highlighted in Subsection III-D, the CSAT successfully reduced the computation time required in the attachment test.

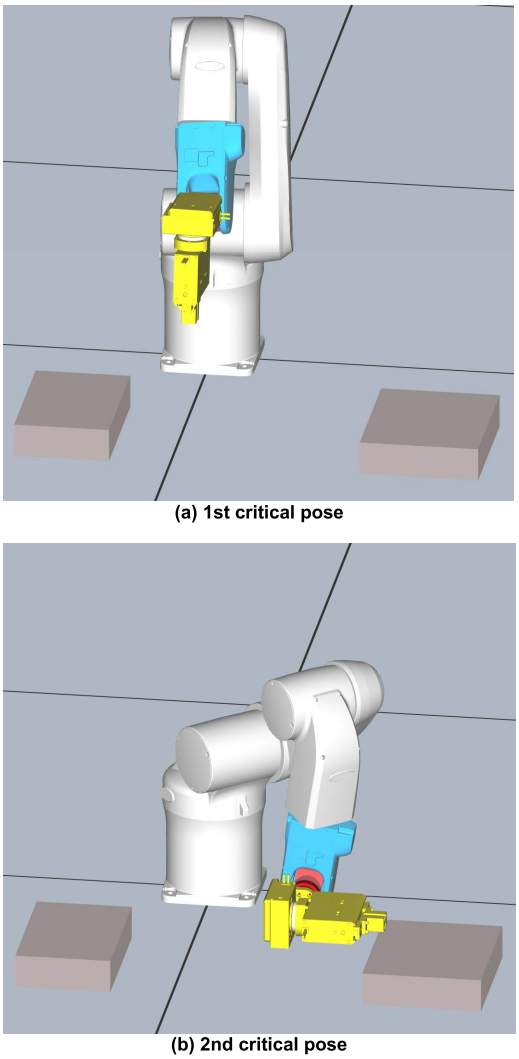

FIGURE 14. Critical pose Θ_2 for C_2 for Motion 2.

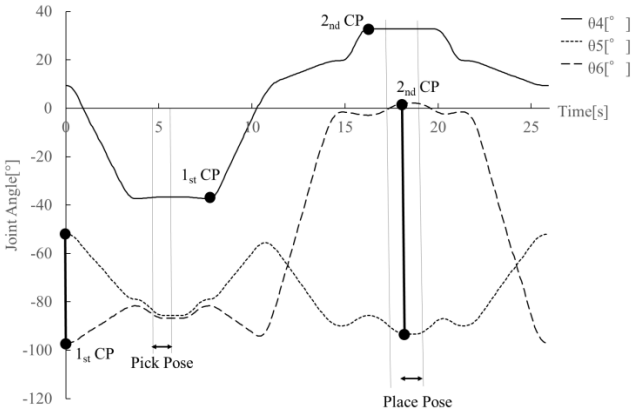

FIGURE 15. Joint angle time series with critical poses (CPs) for Motion 2.

IV. EXPERIMENTS

In the experiments performed on the actual robot arm, the cable was attached to the guide based on the d^* obtained using the cascade structure for the cable path optimization.

TABLE 9. Comparison Of Previous and Proposed Methods.

	Previous method	Proposed method		
Motion	Total time (h)	Attachment test time (min)	Motion test time (min)	Total time (min)
1	20.1	37.4	0.56 (0.08 × 7)	38.0
2	25.6	33.4	0.65 (0.13× 5)	34.1

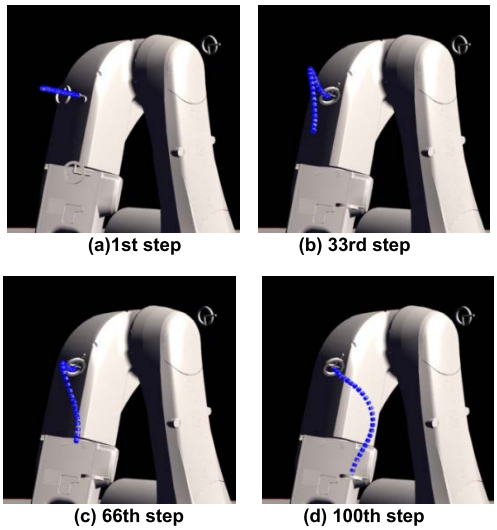

FIGURE 16. Cable geometry simulation of the attachment test.

Fig. 19 shows the cable geometry and surrounding environment at the initial, pick, and place poses in the motion simulation (Figs. 19 (a)–(c)) and experiments (Figs. 19 (d)–(f)) for Motion 1. Similarly, Fig. 20 depicts the simulation images and photographs of the experimental setup for Motion 2. The geometries of the cables generated in the experiments were very similar to those obtained via the simulations for Motions 1 and 2.

A. CABLE GEOMETRY VALIDATION

It was visually validated that the cable did not come into contact with the robot arm and was not stretched during the arm movement. Supplementary videos 1 and 2 show changes in the cable geometry during Motions 1 and 2. Moreover, a radius of the curvature of 52 mm was measured for the place pose, which was the smallest in the simulation for Motion 2 and larger than the threshold $Curvature_{th} = 48$mm.

Now, the cable geometry when the motion speed becomes faster is discussed. If the motion is quite fast, the cable is expected to be swung around, resulting in a considerable difference between the simulated and actual geometries. In our future tasks, to investigate such swinging around of the cable, the faster motion in the simulation will be considered and the simulated and actual geometries in faster motion will be compared using special high-speed video devices.

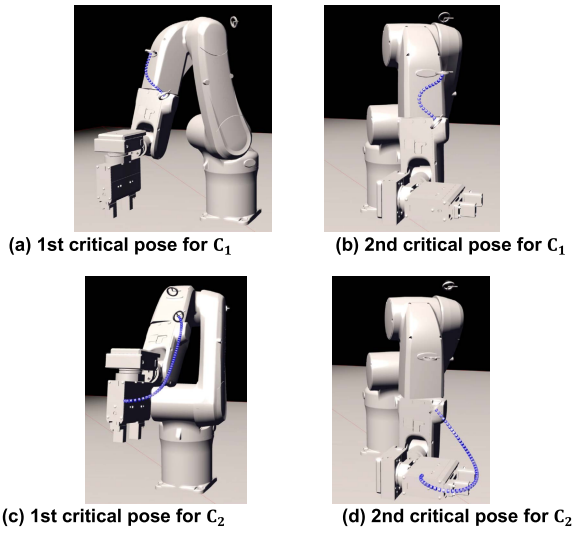

FIGURE 17. Cable segment geometries at critical poses in the attachment simulation of Motion 2.

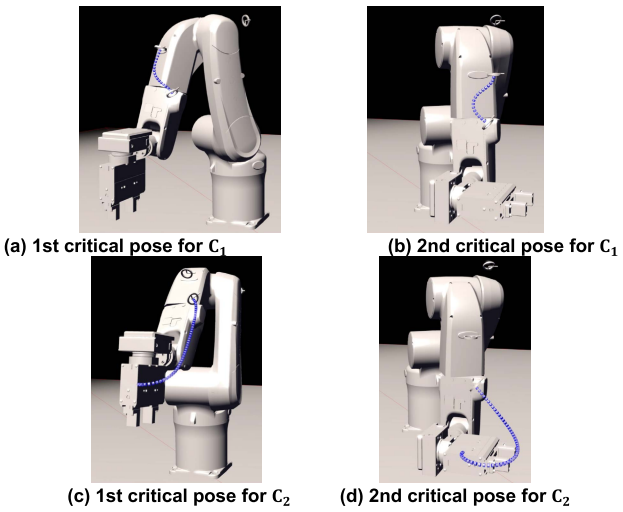

FIGURE 18. Cable segment geometries at critical poses in the motion simulation of Motion 2.

B. COMPARISON OF THE OPTIMAL PVs FOR MOTION 1 AND 2

The differences in the tendencies of the ECPVs for the two motions are discussed. As mentioned in Subsection III-D, the top-ranked ECPVs of D_3 presented in TABLE 8 showed different tendencies: i) the ψ values in P_2 were 0° or 45° in Motion 1, whereas they were 45° in Motion 2. ii) the S_1 values for Motion 1 were slightly larger than those for Motion 2; and iii) the S_2 values for Motion 1 were smaller than those for Motion 2.

First, i) the difference between the ψ values in P_2 is discussed for Motion 1 and 2 based on the optimal cable path at the place poses presented in Figs. 19(c) and 20(c) or Figs. 19(f) and Fig. 20(f), respectively. In Motion 1, the end effector faces downward. Therefore, G_2 mounted on L_4 was optimized downward ($\psi = 0$). Meanwhile, in Motion 2, the end effector faces to the right side. Thus, G_2 must be turned

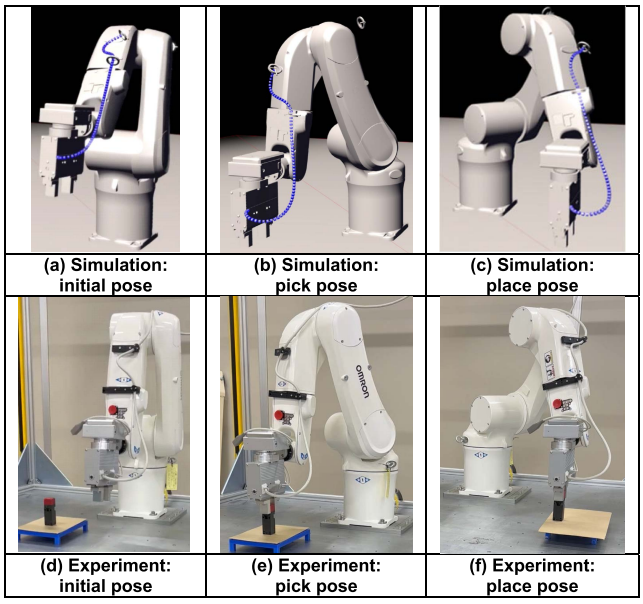

FIGURE 19. Simulated and experimental results for Motion 1, where $\mathbf{d^* = (S_1, S_2, P_1, P_2) = (20{,}47, (0{,}40{,}0{,}0{,}0, -45), (0{,}60{,}20{,}0{,}0{,}0))}$.

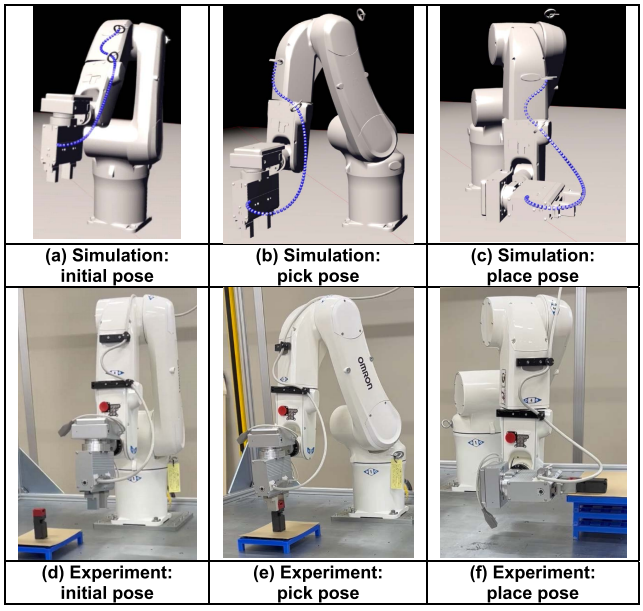

FIGURE 20. Simulated and experimental results for Motion 2, where $\mathbf{d^* = (S_1, S_2, P_1, P_2) = (19{,}48, (0{,}40{,}0{,}0{,}0{,}0), (0{,}60{,}0{,}0{,}0{,}45))}$.

right down ($\psi = 45°$) to guarantee a minimum curvature radius of C_2.

Next, ii) the difference between the S_1 values is discussed for Motion 1 and 2 based on the optimal cable path for the pick poses presented in Figs. 19(b) and 20(b) or Figs. 19(e) and Fig. 20(e), respectively. These pick poses were extracted as the 1st critical poses for C_1 in Motion 1 and 2. $G_1$and G_2 for Motion 1 face away from each other compared with those for Motion 2, yielding a slightly greater S_1 value for Motion 1 than that for Motion 2. It was confirmed that smaller values of S_1could not satisfy the stretch constraint at their pick pose for both the motions.

Finally, iii) the difference between the S_2 values is discussed for Motion 1 and 2 based on the optimal cable path at the initial pose presented in Figs. 19(a) and 20(a) or Figs. 19(d) and Fig. 20(d), respectively. These initial poses were extracted as the 1st critical poses for C_2 for both the motions. Owing to the abovementioned difference of the ψ values in P_2, G_2 for Motion 1 faces toward G_3 more straightly than G_2 for Motion 2, yielding a slightly smaller S_2 values for Motion 1 than that for Motion 2. It was confirmed that smaller values of S_2could not satisfy the stretch constraint at the initial poses for both the motions.

V. CONCLUSION

In this study, an efficient automatic method is proposed for cable path design. In this method, after decomposing the entire cable into cable segments divided by guides, multiple candidate cable paths were represented as a set of PVs that comprised the configuration of the guides and cable length. The optimal PV that provides the shortest cable path and satisfies the stress and robustness constraints was efficiently obtained. Three major new concepts were introduced: critical robot poses, CSAT and a cascade structure for cable path optimization.

To clarify the effectiveness of the proposed method, case studies were conducted on two pick-and-place motions. Based on the definition of the critical pose, multiple critical poses were extracted from the motions. Then, attachment tests were conducted for the critical poses, and they afforded a reduced computation time by decreasing the number of PV candidates in the cascade structure. Motion tests were performed on the ECPV set generated using the obtained PVs. The cable geometry obtained via the attachment simulation for critical poses was comparable to that obtained via the motion simulation. Furthermore, the simulation results on two robot motions indicated that the proposed method drastically reduced the computation time to ∼3% of that obtained using the previous method [23].

In future, the relation between the computation time and the module order will be studied for each cable segment in the CSAT, especially for more than three cable segments. Moreover, reduction of the computation time will be attempted for each attachment test by initializing the cable geometry via spline interpolation.

REFERENCES

[1] *Executive Summary World Robotics 2021 Industrial Robots*, World Robot, Int. Fed. Robot., Frankfurt, Germany, 2021, p. 12.

[2] Y. Domae, "Recent trends in the research of industrial robots and future outlook," *J. Robot. Mechatronics*, vol. 31, no. 1, pp. 57–62, Feb. 2019, doi: 10.20965/jrm.2019.p0057.

[3] L. Sanneman, C. Fourie, and J. A. Shah, "The state of industrial robotics: Emerging technologies, challenges, and key research directions," *Found. Trends Robot.*, vol. 8, no. 3, pp. 225–306, 2021, doi: 10.1561/2300000065.

[4] S. S. Antman, "Background," in *Nonlinear Problems of Elasticity* (Applied Mathematical Sciences), vol. 107. New York, NY, USA: Springer, 2005, pp. 1–10. [Online]. Available: https://link.springer.com/chapter/10.1007/978-1-4757-4147-6_1#preview, doi: 10.1007/978-1-4757-4147-6_1.

[5] J. Spillmann and M. Teschner, "CoRdE: Cosserat rod elements for the dynamic simulation of one-dimensional elastic objects," in *Proc. ACM SIGGRAPH/Eurographics Symp. Comput. Animation (SCA)*, 2007, pp. 63–72.

[6] M. Grégoire and E. Schömer, "Interactive simulation of one-dimensional flexible parts," *Comput.-Aided Des.*, vol. 39, no. 8, pp. 694–707, Aug. 2007, doi: 10.1016/j.cad.2007.05.005.

[7] D. Baraff and A. Witkin, "Large steps in cloth simulation," in *Proc. 25th Annu. Conf. Comput. Graph. Interact. Techn. (SIGGRAPH)*, 1998, pp. 43–54, doi: 10.1145/280814.280821.

[8] E. Hergenröther and P. Dähne, "Real-time virtual cables based on kinematic simulation," Univ. West Bohemia, Plzen-Bory, Czech Republic, Tech. Rep., 2000, pp. 402–409. [Online]. Available: https://www.semanticscholar.org/paper/Real-Time-Virtual-Cables-Based-on-Kinematic-Hergenr%C3%B6ther-D%C3%A4hne/aa6d35de59dcf101531969d79569c3789379035b#citing-papers

[9] A. Loock and E. Schömer, "A virtual environment for interactive assembly simulation: From rigid bodies to deformable cables," in *Proc. World Multiconf. Syst. Cybern. Inform.*, 2001, pp. 325–332. [Online]. Available: http://citeseerx.ist.psu.edu/viewdoc/download?doi=10.1.1.167.4262&rep=rep1&type=pdf

[10] N. Lv, J. Liu, X. Ding, J. Liu, H. Lin, and J. Ma, "Physically based real-time interactive assembly simulation of cable harness," *J. Manuf. Syst.*, vol. 43, pp. 385–399, Apr. 2017, doi: 10.1016/j.jmsy.2017.02.001.

[11] M. Müller, B. Heidelberger, M. Hennix, and J. Ratcliff, "Position based dynamics," *J. Vis. Commun. Image Represent.*, vol. 18, no. 2, pp. 109–118, Apr. 2007, doi: 10.1016/j.jvcir.2007.01.005.

[12] *Bullet Real-Time Physics Simulation*. Accessed: Jun. 14, 2022. [Online]. Available: https://pybullet.org/wordpress/

[13] *Havok Physics*. Accessed: Jun. 14, 2022. [Online]. Available: https://www.havok.com/havok-physics/

[14] SDK. *Physics*. Accessed: Jun. 14, 2022. [Online]. Available: https://developer.nvidia.com/physx-sdk

[15] L. Angel, "Algorithm for computer guidance of a manipulator in between obstacles," Oklahoma State Univ., Stillwater, OK, USA, Tech. Rep., 1973. [Online]. Available: https://shareok.org/handle/11244/23864?show=full

[16] J. T. Schwartz and M. Sharir, "On the 'piano movers' problem. II. General techniques for computing topological properties of real algebraic manifolds," *Adv. Appl. Math.*, vol. 4, no. 3, pp. 298–351, 1983, doi: 10.1016/0196-8858(83)90014-3.

[17] Z. Shiller and S. Dubowsky, "Global time optimal motions of robotic manipulators in the presence of obstacles," in *Proc. IEEE Int. Conf. Robot. Autom.*, Apr. 1988, pp. 370–375, doi: 10.1109/ROBOT.1988.12076.

[18] S. M. LaValle, *Planning Algorithms*. Cambridge, U.K.: Cambridge Univ. Press, 2006, pp. 1–826. [Online]. Available: https://www.cambridge.org/core/books/planning-algorithms/FC9CC7E67E851E40E3E45D6FE328B768, doi: 10.1017/CBO9780511546877.

[19] S. M. LaValle, "Rapidly exploring random trees: A new tool for path planning," Annu. Res. Rep., Iowa State Univ., Ames, IA, USA, 1998. [Online]. Available: http://msl.cs.illinois.edu/~lavalle/papers/Lav98c.pdf

[20] J. Kressin, "Path optimization for multi-robot station minimizing dress-pack wear," Chalmers Univ. Technol. Göteborg, Göteborg, Sweden, Tech. Rep., 2013. [Online]. Available: https://publications.lib.chalmers.se/records/fulltext/179859/179859.pdf

[21] J. S. Carlson, J. Kressin, T. Hermansson, R. Bohlin, M. Sundbäck, and H. Hansson, "Robot station optimization for minimizing dress pack problems," *Proc. CIRP*, vol. 44, pp. 389–394, Dec. 2016, doi: 10.1016/j.procir.2016.01.022.

[22] T. Hermansson, J. S. Carlson, J. Linn, and J. Kressin, "Quasi-static path optimization for industrial robots with dress packs," *Robot. Comput.-Integr. Manuf.*, vol. 68, Apr. 2021, Art. no. 102055, doi: 10.1016/j.rcim.2020.102055.

[23] S. Iwamura, Y. Mizukami, T. Endo, and F. Matsuno, "Cable-path optimization method for industrial robot arms," *Robot. Comput.-Integr. Manuf.*, vol. 73, Feb. 2022, Art. no. 102245, doi: 10.1016/j.rcim.2021.102245.

[24] B. A. Trakhtenbrot, "A survey of Russian approaches to Perebor (brute-force searches) algorithms," *IEEE Ann. Hist. Comput.*, vol. 6, no. 4, pp. 384–400, Oct. 1984, doi: 10.1109/MAHC.1984.10036.

[25] A. H. Land and A. G. Doig, "An automatic method of solving discrete programming problems," *Econometrica*, vol. 28, no. 3, pp. 497–520, Jul. 1960, doi: 10.2307/1910129.

[26] M. L. Puterman, "Dynamic programming," in *Encyclopedia of Physical Science and Technology*. Amsterdam, The Netherlands: Elsevier, Jan. 2003, pp. 673–696. [Online]. Available: https://www.sciencedirect.com/science/article/pii/B0122274105001873?via%3Dihub, doi: 10.1016/B0-12-227410-5/00187-3.

[27] E. B. Paul, "Greedy algorithm," in *Dictionary of Algorithms and Data Structures*, E. B. Paul, Ed. Feb. 2005. [Online]. Available: https://xlinux.nist.gov/dads/HTML/greedyalgo.html and https://www.nist.gov/dads/HTML/greedyalgo.html

[28] Y. Bykov and S. Petrovic, "A step counting Hill climbing algorithm applied to university examination timetabling," *J. Scheduling*, vol. 19, no. 4, pp. 479–492, Aug. 2016, doi: 10.1007/s10951-016-0469-x.
[29] J. Davies and A. Goel, "Visual case-based reasoning II: Transfer and adaptation," in *Proc. 1st Indian Int. Conf. Artif. Intell. (IICAI)*, Hyderabad, India, Dec. 2003, pp. 769–778. [Online]. Available: https://www.researchgate.net/publication/220888064_Visual_Case-Based_Reasoning_II_Transfer_and_Adaptation
[30] M. Mitchell, "An introduction to genetic algorithms," *Sadhana*, vol. 24, nos. 4–5, pp. 293–315, Aug. 1999, doi: 10.1007/BF02823145.
[31] G. Beni and J. Wang, "Swarm intelligence in cellular robotic systems," in *Proc. NATO Adv. Workshop Robots Biol. Syst.*, 1993, pp. 703–712. [Online]. Available: https://link.springer.com/chapter/10.1007/978-3-642-58069-7_38?noAccess=true
[32] A. Qing, "Comment on 'differential evolution as applied to electromagnetics,"' *IEEE Antennas Propag. Mag.*, vol. 53, no. 4, pp. 169–171, Aug. 2011, doi: 10.1109/MAP.2011.6097316.
[33] F. Glover, "Future paths for integer programming and links to artificial intelligence," *Comput. Oper. Res.*, vol. 13, no. 5, pp. 533–549, 1986, doi: 10.1016/0305-0548(86)90048-1.
[34] S. Kirkpatrick, C. D. Gelatt, and M. P. Vecchi, "Optimization by simulated annealing," *Science*, vol. 220, no. 4598, pp. 671–680, 1983, doi: 10.1126/science.220.4598.671.
[35] M. L. R. Chandra, B. V. Kumar, and B. S. Babu, "IoT enabled home with smart security," in *Proc. Int. Conf. Energy, Commun., Data Anal. Soft Comput. (ICECDS)*, Aug. 2017, pp. 1193–1197, doi: 10.1109/ICECDS.2017.8389630.
[36] Y. Freund and R. E. Schapire, "A decision-theoretic generalization of on-line learning and an application to boosting," *J. Comput. Syst. Sci.*, vol. 55, no. 1, pp. 119–139, Aug. 1997, doi: 10.1006/jcss.1997.1504.
[37] A. Kasinski and A. Schmidt, "The architecture of the face and eyes detection system based on cascade classifiers," in *Computer Recognition Systems 2* (Advances in Soft Computing), vol. 2. Berlin, Germany: Springer, 2007, pp. 124–131. [Online]. Available: https://link.springer.com/chapter/10.1007/978-3-540-75175-5_16, doi: 10.1007/978-3-540-75175-5_16.
[38] S. Paisitkriangkrai, C. Shen, and J. Zhang, "Fast pedestrian detection using a cascade of boosted covariance features," *IEEE Trans. Circuits Syst. Video Technol.*, vol. 18, no. 8, pp. 1140–1151, Aug. 2008, doi: 10.1109/TCSVT.2008.928213.
[39] P. Negri, X. Clady, S. M. Hanif, and L. Prevost, "A cascade of boosted generative and discriminative classifiers for vehicle detection," *EURASIP J. Adv. Signal Process.*, vol. 2008, no. 1, Dec. 2008, Art. no. 782432, doi: 10.1155/2008/782432.
[40] S. U. Sharma and D. J. Shah, "A practical animal detection and collision avoidance system using computer vision technique," *IEEE Access*, vol. 5, pp. 347–358, 2017, doi: 10.1109/ACCESS.2016.2642981.
[41] B. Yuan, H. Du, H. Wang, and W. Xiong, "The simulation of cable harness based on mass-spring model," in *Proc. MATEC Web Conf.*, vol. 31, 2015, pp. 1–4, doi: 10.1051/matecconf/20153110002.
[42] *Omron Viper*. Accessed: Jun. 14, 2022. [Online]. Available: http://www.ia.omron.com/products/family/3520/download/catalog.html
[43] *SMC LEHF32EK2-32*. Accessed: Jun. 14, 2022. [Online]. Available: http://ca01.smcworld.com/catalog/Electric/mpv/Electric-LEH/data/Electric-LEH.pdf
[44] *SMC LE-CP-3*. Accessed: Jun. 14, 2022. [Online]. Available: http://ca01.smcworld.com/catalog/Electric/mpv/Electric-LEC-JXC/data/Electric-LEC-JXC.pdf
[45] *Omron Sysmac Studio*. Accessed: Jun. 14, 2022. [Online]. Available: https://automation.omron.com/en/us/products/family/sysstdio

SHINTARO IWAMURA received the M.E. degree in electrical engineering from Yamaguchi University, Yamaguchi, Japan, in 2006. He is currently pursuing the Ph.D. degree with the Department of Mechanical Engineering, Kyoto University, Kyoto, Japan. He has been working as a Software Developer at Omron Corporation, since 2006. He develops PC applications for industrial automation and robotics. His research interests include industrial robot and digital transformation for factory automation.

YOSHIKI MIZUKAMI (Member, IEEE) received the Ph.D. (Dr. Eng.) degree from the Graduate School of Sciences and Engineering, Yamaguchi University, in 1998. He was a Researcher with the Venture Business Laboratory, Yamaguchi University, from 1998 to 1999. He was an Assistant Professor in electrical and electronic engineering with Yamaguchi University, from 1999 to 2008, where he has been an Associate Professor with the Graduate School of Sciences and Technology for Innovation, since 2008. He was a Visiting Researcher with University College London, from 2009 to 2010. His research interests include image processing, artificial intelligence, educational software development, and robot technology. He is a member of the Institute of Electronics, Information and Communication Engineers (IEICE), the Institute of Systems, Control and Information Engineers (ISCIE), and Information Processing Society of Japan (IPSJ).

TAKAHIRO ENDO (Member, IEEE) received the Ph.D. (Dr. Eng.) degree from the Tokyo Institute of Technology, Japan, in 2006. He was an Assistant Professor with Gifu University, Gifu, Japan. Since April 2015, he has been with the Department of Mechanical Engineering and Science, Kyoto University, Kyoto, Japan, where he is currently an Associate Professor. His research interests include haptics, robotics, and control of infinite-dimensional systems.

FUMITOSHI MATSUNO (Senior Member, IEEE) received the Ph.D. (Dr. Eng.) degree from Osaka University, in 1986. In 1986, he joined the Department of Control Engineering, Osaka University. Since 2009, he has been a Professor with the Department of Mechanical Engineering and Science, Kyoto University. He also holds a post of the NPO International Rescue System Institute (IRS). He worked as the President of the Institute of System, Control and Information Engineers (ISCIE) and the Vice-President of Robotics Society of Japan (RSJ). His current research interests include robotics, swarm intelligence, control of distributed parameter system and nonlinear systems, and rescue support system in disaster. He received many awards, including the Outstanding Paper Award from the Society of Instrument and Control Engineers (SICE), in 2001, 2006, and 2017, the Prize for Academic Achievement from Japan Society of Mechanical Engineers (JSME), in 2009, the Best Paper Award from Information Processing Society of Japan, in 2013, and the Best Paper Award from RSJ, in 2018. He is a Fellow Member of the SICE, the JSME, and the RSJ.